Applied Ocean Research 161 (2025) 104645

Contents lists available at ScienceDirect

Applied Ocean Research

journal homepage: www.elsevier.com/locate/apor

Research Paper

The effects of vorticity and turbulence on the wave-induced drift of bluff bodies in numerical simulations

Qian Xiao [a],*, Shiqiang Yan [b], Thomas A.A. Adcock [a], Ton S. van den Bremer [a,c]

[a] Department of Engineering Science, University of Oxford, Oxford, OX1 3PJ, UK
[b] School of Science and Technology, City, University of London, London, EC1V 0HB, UK
[c] Department of Civil Engineering and Geosciences, TU Delft, Stevinweg 1, 2628 CN Delft, The Netherlands

ARTICLE INFO

Keywords:
Enhanced drift
Wave-induced drift
Vorticity
Bluff bodies

ABSTRACT

Under the influence of surface gravity waves, a floating object experiences a drift in addition to its oscillatory motion. Due to its inertia, both the object's oscillatory motion and its drift will experience a deviation from that of a fluid particle, with the drift of the object typically exceeding the Stokes drift of a fluid particle. This study uses two-dimensional numerical simulations to examine the drift of floating objects in unidirectional, regular, deep-water waves. We investigate the effects of vorticity and turbulence induced by different object shapes. We consider two corner shapes: sharp and round. We investigate object sizes ranging from 1% to 10% of the wavelength. Three types of (two-dimensional) numerical simulations are performed to explore the roles played by viscosity and turbulence: simulations based on the Reynolds-Averaged Navier–Stokes equations (RANS), viscid simulations using the Navier–Stokes equations, and inviscid simulations solving the Euler equations. Objects smaller than 4% of the wavelength are predicted to have a drift equal to the Stokes drift for both corner shapes. As size increases, objects with sharp corners exhibit greater drift enhancement compared to round-cornered objects of equivalent size (compared to the Stokes drift, we report a 454% increase for a sharp-cornered box and a 134% increase for a round-cornered box, both with an object size of 10% of the wavelength). In addition to differences in diffraction patterns and phase differences in the linear motion between objects with two different shapes, a new mechanism for drift enhancement, which is caused by the vorticity generated by the sharp corners, has been identified. The vorticity that arises due to the sharp corners is asymmetrically distributed between the two sides of the object, leading to a non-symmetric dynamic pressure field and, thereby, mean horizontal forces in the direction of wave propagation. The influence of viscosity and turbulence on drift is explored. Viscosity is found to play a dual role. On the one hand, it induces a phase difference in the linear motion and thus increases the drift. On the other hand, viscosity reduces vorticity and thereby decreases the drift enhancement. Finally, we define an unsteadiness ratio of object drift to examine the effect of non-zero acceleration, revealing a correlation between unsteadiness and drift enhancement.

1. Introduction

Flow around bluff bodies is a topic that has attracted considerable interest and has been extensively explored in various engineering applications over many decades. Bluff-bodied structures, including skyscrapers, bridges, wind turbines and (floating) ocean platforms, are surrounded by highly unsteady flow fields, characterized by phenomena such as flow separation, shear-layer instability, and vortex shedding and reattachment. These phenomena not only impact the aerodynamic/hydrodynamic characteristics of the structure but also affect the forces and motions experienced by them. Pioneering work on the flow around square cylinders (i.e., a three-dimensional geometric shape that has a square base and top, and its side faces are rectangles) was conducted by Roshko (1952), Lyn et al. (1995), Wiliamson (1996), who investigated vortex shedding and the properties of the turbulent flow. More recently, researchers such as Yoon et al. (2010), Yen and Yang (2011), Chen and Xia (2017) performed numerical and experimental studies to explore different flow patterns, including flow separation, vortex formation and reattachment, across various Reynolds numbers and their effects on flow-induced forces.

Much effort has been made to investigate the influence of different cross-sectional shapes and corner radii on flow features and flow-induced loads. Delany and Sorensen (1953) carried out an experimental

* Corresponding author.
E-mail address: qian.xiao@eng.ox.ac.uk (Q. Xiao).

https://doi.org/10.1016/j.apor.2025.104645
Received 16 May 2024; Received in revised form 11 February 2025; Accepted 20 May 2025
Available online 18 June 2025

study for different cross-sectional shapes, including rectangular, elliptical, and diamond shapes, with different corner radii, and explored the corresponding variation in drag coefficients for different Reynolds numbers. For Reynolds numbers of 10^5, the drag coefficient remains essentially constant or decreases with an increase of the corner radius. Bearman et al. (1984) presented experimental measurements using U-tube water tunnel and investigated the effects of corner radius on hydrodynamic forces and loads on bluff bodies with Reynolds numbers ranging from 200 to 2×10^4 and Keulegan–Carpenter (KC) numbers ranging from 1 to 100. They reported that sharp-cornered bodies experience flow separation at lower KC values compared to circular shapes, and the drag coefficient is reduced with increasing corner rounding, especially at relatively high KC numbers. This reduction is more evident in oscillatory flow than in steady flow and is highly sensitive to the corner radius.

Tamura et al. (1998) used a Computational Fluid Dynamics (CFD) model without incorporating a turbulence model to investigate the relationship between flow structure, vortex formation, and unsteady pressure. They explored various corner shapes (e.g., sharp corners, chamfered corners, and round corners) and compared their numerical simulations with experimental measurements. Tamura et al. (1998) found that slight changes in corner shape could drastically modify the pressure distribution on the rectangular cylinder (i.e., a three-dimensional geometric shape that has a rectangular base and top, and its side faces are rectangles) surface and affect drag. The effect of corner modification on forces on the object in different turbulent flows was investigated further in experiments by Tamura and Miyagi (1999). They explained that decreased drag arose due to rounding of the corners as a result of different separation patterns and extents of reattachment. Hu et al. (2006) put their focus on the near-wake structure and experimentally investigated the influence of different corner radii. They found that an increase in the corner radius leads to a decrease in vortex-shedding strength and vortex-relevant circulation. Sharp-cornered structures exhibit a lower quasi-periodic vortex-shedding frequency than other objects. Moreover, Hu et al. (2006) emphasized that the leading-edge corner radius is most important, as it determines to a great extent the behaviour of streamlines, separation angle, pressure on the base of the object, and near-wake structure. Liang et al. (2016) used Detached Eddy Simulation to simulate the vortex-induced motions of four square cylinders in uniform flow and compared the results with experiments. The cross-sectional shapes of their cylinders were all diamonds with small round-cornered radii. They found that the flow characteristics around the downstream cylinders are strongly affected by the vortices induced by the upstream cylinders.

Despite extensive research on bluff bodies in steady or unsteady flows described above, none of the above studies considered the presence of a free surface. However, for problems involving structures, such as hydrofoils, offshore platforms, wave energy converters, and other surface-piercing objects, the presence of a free surface introduces additional complexity, such as the generation of waves and their interaction with boundary layers, vortices and bubbles. The effects of the free surface and the surface waves generated for surface-piercing cylinders have been studied by several authors (Inoue et al., 1993; Kawamura et al., 2002; Lin and Li, 2003). These authors found that the strength and frequency of vortex shedding are reduced, while a different instability mechanism with more random fluctuations of higher frequency dominates in the region near the surface. Kandasamy et al. (2005) employed Reynolds-Averaged Navier–Stokes (RANS) simulations with complementary experiments to investigate the unsteady flow pattern of free surface wave-induced separation for two different Froude numbers. They found that the formation of shear-layer vortices is also impeded by the presence of the free surface. However, it is important to note that the water surface in those studies is initially calm without waves, and waves are only induced by the motion of the object as the fluid flows past the object.

In the ocean environment, structures often encounter both a mean flow and free surface waves. Wave run-up around surface-piercing cylinders has been extensively explored both numerically and experimentally (Stansberg and Nielsen, 2001; Stansberg and Kristiansen, 2005; Stansberg et al., 2005; Danmeier et al., 2008; Huang et al., 2008; Bøckmann et al., 2014). Recently, Yoon et al. (2016) and Mohseni et al. (2018) have conducted unsteady RANS simulations of wave run-up on surface-piercing cylinders in regular waves of different wavelengths and wave steepnesses. They found that, compared to wave steepness, wavelength (relative to object size) is the major factor influencing wave-induced loads. Longer waves are more prone to developing vortex shedding, and the size of the vortices is highly related to the KC number. Moreover, the difference in the velocity direction between the crest and the trough disturbs the regular structure of the vortex shedding, especially in low-KC cases. Moradi et al. (2015) simulated wave-induced fluid-flow resonance in narrow gaps between two fixed surface-piercing bodies over a variety of incident wave frequencies and evaluated the effects of geometry properties (e.g., different corner shapes) of the object on gap-resonance characteristic. They showed that changes in corner shape significantly affect the wave elevation in the gap during resonance by altering the amount of water trapped in the gap. For sharp-cornered objects, the wave height during resonance reduces significantly due to large-scale vortex structure and kinetic energy dissipation.

Vortical structures observed in simulations using the Volume of Fluid-RANS model of Palm et al. (2016) are similar across different wave periods, and no wake was found. According to Palm et al. (2018), vorticity generated in the flow modifies the driving wave pressure distribution and can cause separation, resulting in a reduction of wave force amplitude. Palm et al. (2018) found that for geometries with sharp edges (e.g., sharp-cornered objects), regions of sharp pressure gradients induce drag that is dominated by geometrically induced vorticity, while viscosity plays a less important role.

Despite extensive research on the effects of vorticity and turbulence on surface-piercing objects that are either fixed or moored in flows with waves, relatively little work has been done for freely floating objects, which typically undergo net drift in the direction of wave propagation. For an idealized fluid parcel in a flow without a Eulerian-mean current, this drift is equal to Stokes drift (Stokes, 1847). Since Stokes first described this drift, now 177 years ago, it has been widely explored in experimental and theoretical studies (see Van den Bremer and Breivik (2018) for a review). However, as Stokes drift is derived for an idealized fluid particle based on ideal-fluid and irrotational-flow assumptions, it may not accurately predict the drift of a freely floating object in the real ocean. Ignoring the Earth's rotation, which becomes relevant only for large spatial and temporal scales, there are four main factors affecting the drift. First, wave breaking has been shown to increase drift at the wave surface compared to non-breaking waves and may alter Lagrangian transport in realistic wave fields (Deike et al., 2017; Sinnis et al., 2021; Eeltink et al., 2023). Second, the presence of viscosity may lead to additional drift due to velocity streaming within the boundary layer beneath the water surface (Longuet-Higgins, 1953; Grue and Kolaas, 2017). Vorticity from the boundary layers may be advected or diffused into the interior of the fluid, affecting the transport of particles (Longuet-Higgins, 1953). Third, inertial objects of non-negligible size exhibit non-Lagrangian drift behaviour (Calvert et al., 2021; DiBenedetto et al., 2022). Drift enhancement for inertial objects has been found for objects with sizes larger than several percent of the wavelenghth and such enhancement can vary depending on the objects' shape (Calvert et al., 2021). Fourth, diffraction effects caused by the presence of objects can induce drift enhancement for relatively large objects. Xiao et al. (2024a) introduced a diffraction-modified Stokes drift to predict the enhanced drift resulting from diffraction. They observed that the drift enhancement is closely linked to a standing-wave pattern generated by wave diffraction. This diffraction-related mechanism for drift enhancement is further supported by the laboratory

study of Xiao et al. (2024b). The effects of size, shape, wave steepness and viscosity on an objects' drift are explored in Xiao et al. (2024a). However, in their study, the object's shape was always chosen to be round-cornered in order to avoid the generation of vorticity due to sharp gradients of the geometry, that is, sharp corners.

This paper aims to investigate the effects of vorticity and turbulence induced by the geometry of the object along with the effects of viscosity on the forces and mean drift velocity of freely floating objects of different sizes and for different wave steepnesses. The geometry of the object is varied by considering two different corner shapes (sharp and round). Velocity and pressure fields, as well as vortex structures, are analysed. We use the two-dimensional hybrid numerical model, QaleFOAM (Li et al., 2018; Yan et al., 2019; Gong et al., 2020), and conduct three types of simulations for each case, which respectively solve the RANS, Navier–Stokes (viscid) and Euler (inviscid) equations (henceforth, the RANS, Navier–Stokes and Euler simulations) to investigate the effects of viscosity and turbulence. We report significant differences in the mean drift of relatively large objects with sharp corners compared to round-cornered objects. This paper is an extension of Xiao et al. (2024a,b). It uses the same numerical model as Xiao et al. (2024a) and compares to the results for objects with round corners therein. The experimental data from Xiao et al. (2024b) are used for comparison. For completeness, we note that the RANS and Navier–Stokes simulations in Xiao et al. (2024a) gave nearly identical results for drift of objects with round corners; we do not revisit these results herein.

2. Numerical model

The hybrid numerical model QaleFOAM is employed in this paper; it is based on a domain-decomposition method and couples a fully nonlinear potential-flow solver, QALE-FEM (Quasi Arbitrary Lagrangian-Eulerian Finite Element Method), with a two-phase incompressible Navier–Stokes solver. The hybrid numerical domain of QaleFOAM along with the object location are shown in Fig. 1. The region of interest, typically near the object and referred to as the Navier–Stokes domain, encompasses small-scale complex physics and is modelled using the two-phase incompressible InterDyMFoam solver available within OpenFOAM. This solver employs the Volume of Fluid (VoF) method to discern the interface between two fluids. Conversely, the larger region, termed the QALE-FEM domain, is used to simulate wave propagation and evolution and employs the QALE-FEM potential-flow solver. One-way coupling scheme is adopted, in which the QALE-FEM solver provides wave solutions to the InterDyMFoam solver at the coupling interfaces but does not feed any solutions back. Wave generation and absorption are implemented within the QaleFOAM solver with wave absorbers deployed at the interfaces of the two models to manage reflected and radiated waves. Given the two-dimensional nature of the calculations, the front and back boundaries of the Navier–Stokes model are turned off. For further details of the QaleFOAM solver, readers are referred to Li et al. (2018), Yan et al. (2019), Gong et al. (2020) and Xiao et al. (2024a) and related references therein. In the InterDyMFoam solver, there are inlet, outlet, bottom, atmosphere, and body surface boundaries over which we need to define the boundary conditions (BC) for the variables we compute: volume phase fraction α, pressure p and velocity $\mathbf{u} = (u, w)$. The detailed boundary-condition types are given in Table 1 (see the caption for an explanation of the terms), where a no-flow, free-slip condition (*slip*) is used for the bottom, as we study waves in deep water. Following Moradi et al. (2015), we use the divergence scheme $GaussMUSCL$ for the advection term in the momentum equation. The discretization schemes that we use in our model are listed in Table 2. The $PIMPLE$ algorithm is used for velocity–pressure coupling. We use an adjustable time step controlled by the maximum Courant number $\mathrm{Co} = \frac{\Delta t|\mathbf{u}|}{\Delta x}$, in which $|\mathbf{u}|$ refers to the absolute velocity in the flow, and Δt and Δx are the time and space resolutions, respectively. The maximum Courant number is given by $\mathrm{Co} = 0.25$. The effect of surface tension is ignored in all our simulations. A convergence study and a validation and verification of the numerical model are given in Appendices A and B, respectively.

This paper presents three types of simulations: RANS simulations , which respectively solve the RANS, Navier–Stokes (viscid) and Euler (inviscid) equations (henceforth, RANS, Navier–Stokes and Euler simulations). In the Reynolds averaged Navier–Stokes (RANS) simulations, following Yu and Li (2013) and Li et al. (2018), we use a k–ω SST turbulence model. Due to the importance of accurately predicting forces for evaluating drift, we use a wall-resolving treatment for near-wall regions. As required by the wall-resolving treatment, the boundary conditions on the body surface are set as follows: the kinetic turbulent energy k_e is initialized with a very small value 1.0×10^{-12} with the boundary condition set as the $fixedValue$ type; the turbulent viscosity ν_t is $calculated$ with an initial value 0 and the turbulent specific dissipation rate ω is initialized using a $fixedValue$ condition with a value calculated by $\omega = \frac{60\nu}{0.075y^2}$, in which y is the distance to the first cell centre normal to the wall. We have conducted sensitivity tests of different boundary conditions for wall conditions (including of low-Reynolds number wall functions and of high-low Reynolds number blended wall functions) with various initial values. However, these tests have shown little impact on the results, as our near-wall mesh is sufficiently fine, ensuring that the non-dimensional wall distance $y^+ < 1$ and the first-layer wall cell is always located in the viscous sublayer. Navier–Stokes simulations solve the incompressible Navier–Stokes equations without any turbulence model. Euler simulations are based on incompressible Euler equations, which are compared with RANS and Navier–Stokes simulations to identify the effect of viscosity. Although Euler simulations do not include viscosity, they support flow rotation (i.e., vorticity). Despite their inability to model boundary-layer separation effects due to the absence of near-wall shear stress, Euler equations are widely used to study the vorticity generated in regions with high pressure and velocity gradients such as those induced by high wall curvature (Spalart, 1998; Yang et al., 2007; Palm et al., 2018). This geometrically induced vorticity is inherently triggered by the numerical viscosity from the discretization. Comparison between the three types of simulations (RANS, Navier–Stokes and Euler) allows us to assess the effects of viscosity, vorticity and turbulence.

In the present paper, we investigate the flow dynamics around a two-dimensional (2D) bluff body floating on the water surface in the presence of incoming waves but in the absence of a mean current. We consider two types of objects: stationary objects and moving objects. To better characterize our problem, we introduce the particle Reynolds number (Re), which is different from the Reynolds number of the flow itself, and the Keulegan–Carpenter (KC) number separately for each type of object. For moving objects, we follow Xiao et al. (2024a) and define a particle Reynolds number Re_x by using the characteristic length of the object, denoted as l (equal to the length of the object), and the horizontal velocity difference between the object and the fluid: particle $\mathrm{Re}_x = |u_{o,x} - u_{f,x}|l/\nu$. Here, $u_{o,x}$ and $u_{f,x}$ denote the magnitudes of the horizontal velocities of the object and the fluid, respectively, and ν is the kinematic viscosity of the fluid. We estimate $u_{f,x} = a_w\omega_e e^{-kh_d}$ and $u_{o,x} = A_x\omega_e$, where a_w is the wave amplitude, ω_e is the wave angular frequency, k is the wave number, h_d is the submergence (draft) of the object and A_x is the magnitude of the horizontal oscillatory motion of the object. The KC number is defined as $\mathrm{KC} = |u_{o,z} - u_{f,z}|T/h_d$, where $u_{o,z}$ and $u_{f,z}$ denote the magnitude of the vertical velocity of the object and the fluid, respectively, and $T = 2\pi/\omega_e$ is the wave period. We estimate $u_{f,z} = a_w\omega_e e^{-kh_d}$ and $u_{o,z} = A_z\omega_e$, where A_z is the magnitude of the vertical oscillatory motion of the object. For stationary objects, the particle Reynolds and KC numbers are obtained by setting $u_{o,x} = 0$ and $u_{o,z} = 0$, since the object is stationary. The Reynolds number measures the ratio of inertial forces to viscous forces, with laminar flow dominating at low Reynolds numbers and turbulent flow at high Reynolds numbers, which thereby helps predict flow patterns and vortex structures. On the other hand, the KC number

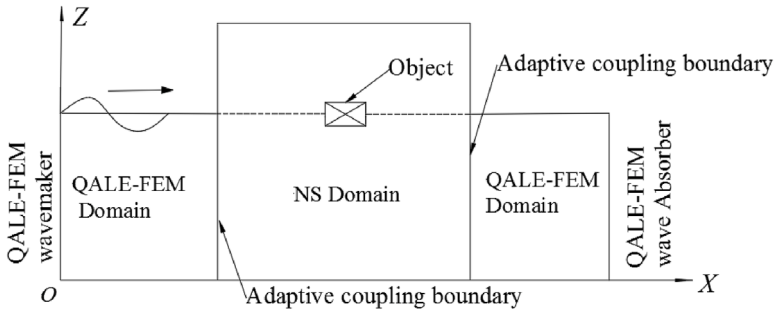

Fig. 1. Schematic of the domains and object location in hybrid QaleFOAM model. *Source:* From Xiao et al. (2024a).

Table 1
Setup of boundary conditions for different variables in our numerical simulations. α is the volume phase fraction, p represents the pressure and **u** denotes the velocity field. The conditions in italics are the standard conditions available in the OpenFOAM platform and the 'Coupled' conditions represent the boundary conditions that are coupled with the QaleFEM solver. The boundary conditions, as described in the OpenFOAM official user guide and manual, are as follows: '*inletOutlet*' serves as a generic outflow condition, allowing for specified inflow when there is return flow; '*totalPressure*' establishes a total pressure condition; '*fixedFluxPressure*' sets the pressure gradient to a provided value such that the flux on the boundary matches the specified velocity boundary condition; '*pressureInletOutletVelocity*' is a velocity inlet/outlet boundary condition applied to pressure boundaries where pressure is specified. For outflow, a zero-gradient condition is applied based on the flux, while for inflow, the velocity is determined from the patch-face normal component of the internal-cell value; '*slip*' refers to a no-flow, free-slip condition (*slip*); '*noSlip*' restrains velocity to zero at walls; '*movingWallVelocity*' provides a velocity value for moving walls. For the object surface, we use three different types of velocity boundary conditions for different types of simulations: *movingWallVelocity* is used for moving objects (for both the Navier–Stokes and the Euler simulations), *noSlip* is used for stationary objects in the Navier–Stokes simulations, and *slip* is used for Euler simulations of stationary objects.

Boundary	α	p	**u**
Inlet	Coupled	*fixedFluxPressure*	Coupled
Outlet	Coupled	*fixedFluxPressure*	Coupled
Bottom	*zeroGradient*	*zeroGradient*	*slip*
Atmosphere	*inletOutlet*	*totalPressure*	*pressureInletOutletVelocity*
Body surface	*zeroGradient*	*fixedFluxPressure*	*movingWallVelocity/noSlip/slip*

Table 2
Discretization schemes used in our numerical simulations, where t and **u** refer to time and velocity, respectively; ρ denotes the fluid density, ϕ refers to the mass flux across the cell faces (i.e., the mass flow rate per unit area across a cell face); for an incompressible fluid, it is replaced by the velocity. α is the volume fraction and α_{rb} is related to an artificial compression term. ϕ_{rb} is the mass flux related to α_{rb}. Turbulent modelling-related terms refer to the convection terms of turbulent kinetic energy (TKE) k_e and the specific rate of dissipation ω in RANS simulations. μ_{eff} is the effective dynamic viscosity, which encompasses both the molecular dynamic viscosity and the turbulent viscosity. The column 'Setup in OpenFOAM' corresponding to the terms used in *fvSchemes* (a setup file name) in OpenFOAM. The schemes in italics are standard schemes available in OpenFOAM.

Terms	Symbol	Setup in OpenFOAM	Schemes
Temporal	$\partial/\partial t$	ddtSchemes	*CrankNicolson*0.9
Gradient terms	∇	gradSchemes	*cellMDLimitedGausslinear*1
Momentum advection term	$\nabla\cdot(\rho\phi\mathbf{u})$	div(rhoPhi,U)	*GaussMUSCL*
Phase fraction-related terms	$\nabla\cdot(\phi\alpha)$	div(phi,alpha)	*GaussvanLeer*
	$\nabla\cdot(\phi_{rb}\alpha)$	div(phirb,alpha)	*GaussinterfaceCompression/Gausslinear*
Turbulence modelling-related terms	$\nabla\cdot(\phi k_e)$	div(phi, k_e)	*GausslinearUpwindlimitedGrad*
	$\nabla\cdot(\phi\omega)$	div(phi,omega)	*GausslinearUpwindlimitedGrad*
Viscosity term	$\nabla\cdot\mu_{eff}\nabla\mathbf{u}$	div((muEff*dev(T(grad(U)))))	*Gausslinear*
Diffusive terms	$\nabla\cdot(\nabla)$	laplacianSchemes	*Gausslinearcorrected*

describes the relative importance of drag forces compared to inertial forces. A small KC number suggests inertia dominates, while a large KC number indicates the drag forces being more important. The KC number can be interpreted as the ratio of the travel distance of fluid particles to the length of the object, thus indicating the likelihood of boundary-layer separation.

We use objects with two corner types: round and sharp. Their dimensions are illustrated in Fig. 2 with values given in Table 3, where l represents the object's length, h is the height, and h_d is the draft. For objects of different shapes but equal size (i.e., length l), we maintain equal density and draft. The second moment of inertia differs slightly between the two shapes; this small difference probably only has a minor effect on the object's motion, as the rotational degree of freedom was found to be unimportant by Xiao et al. (2024a). A non-uniform density distribution could have been used to obtain a second moment of inertia that is equal for the two object shapes. We do not explore this possibility, as this would make comparison with numerical simulations in Xiao et al. (2024a) and experiments in Xiao et al. (2024b), which both have a uniform density distribution, harder.

3. Results

To explore the effects of vorticity and turbulence induced by the geometry of the object on the drift behaviour of floating objects of

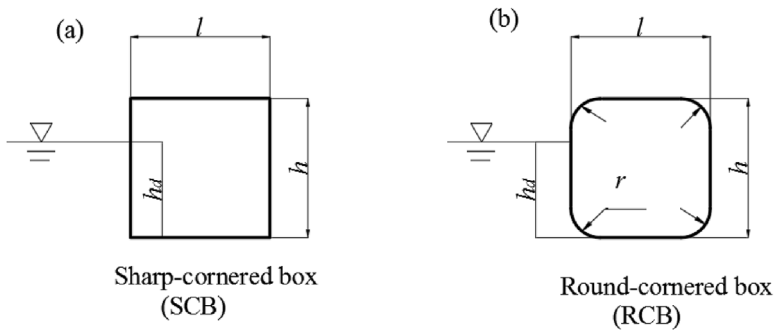

Fig. 2. Shapes and dimensions of the objects with two different corner types: (a) Sharp-cornered boxes (SCBs) and round-cornered boxes (RCBs).

Table 3
Object dimensions of sharp-cornered boxes and round-cornered boxes with a constant density of $\rho = 781$ kg/m^3 and aspect ratio $h_d/l = 0.67$.

SCB & RCB	l/λ (%)	1.0	2.0	3.0	4.0	5.0	6.0	7.0	8.0	9.0	10.0
	l (m)	0.037	0.07	0.11	0.15	0.19	0.22	0.26	0.29	0.33	0.37
	h_d (m)	0.025	0.05	0.075	0.10	0.13	0.15	0.18	0.20	0.23	0.25
	h (m)	0.055	0.08	0.105	0.13	0.16	0.19	0.22	0.26	0.29	0.32
SCB	r (m)	0	0	0	0	0	0	0	0	0	0
RCB		0.006	0.012	0.018	0.024	0.03	0.036	0.043	0.048	0.054	0.06

Table 4
Mean values of y^+ for Navier–Stokes and RANS simulations of sharp-cornered boxes. The mean value is obtained by averaging the time-averaged (over the whole simulation duration) y^+ value over the body surface of the object.

l/λ	1.0	2.0	3.0	4.0	5.0	6.0	7.0	8.0	9.0	10.0
Navier–Stokes	0.22	0.26	0.34	0.38	0.42	0.46	0.48	0.51	0.58	0.63
RANS	0.21	0.29	0.23	0.45	0.42	0.44	0.47	0.51	0.55	0.59

different sizes, we consider objects with two different shapes (cf. Fig. 2). For each shape, we vary the size of the objects systematically. The wave condition used for moving objects is $a_w = 0.02$ m, $\epsilon = ka_w = 0.034$ (ϵ is the wave steepness), $\lambda = 3.69$ m. To present our results, we introduce two dimensionless parameters that describe shape and size: the relative object size, defined as l/λ, and the relative radius of the corners of the round-cornered box, defined as r/h_d, where r is the radius of the round corners. Throughout our simulations, the relative size of the objects ranges from 1% to 10% in 1%-point steps, while the relative radius of the corners of the round-cornered box remains constant at $r/h_d = 0.24$. Detailed dimensional parameters are provided in Table 3. We maintain a fixed box density of $\rho = 781$ kg/m^3 and aspect ratio $h_d/l = 0.67$. The width of the round-cornered boxes is set equal to their height, while the width of the sharp-cornered boxes is adjusted to ensure equivalent mass to their round-cornered counterparts. The mass and moment of inertia of these objects in Table 3 can be easily calculated and are not provided here. To avoid green-water impact, it is essential to ensure the freeboard of the object exceeds the local wave amplitude. However, if we maintain the density and aspect ratio of the object, for a relative size smaller than 5%, the freeboard becomes less than 0.03 m, which is the minimum value to avoid green water if we consider an incident wave amplitude of $a_w = 0.02$ m, which is locally enhanced. Therefore, we set the freeboard of those objects to be at least 0.03 m, which creates a further problem. Boxes with such dimensions are not hydro-dynamically stable. We therefore constrain the rotation for object with a relative size $l/\lambda \leq 5\%$. Considering the constant ratio of submergence depth to size h_d/l, we anticipate that this constraint only leads to differences in the results (Xiao et al., 2024a).

To obtain a range of relative size l/λ, we vary the object size l rather than the incident wavelength λ for two reasons. First, maintaining a constant wavelength (frequency) ensures consistent wave properties encountered by the different objects, which is particularly crucial for comparison with laboratory experiments. By changing the object size, we can use wave frequencies that exhibit desirable wave properties in a tank, such as minimal lateral variation of the wave field and low reflection coefficients. Second, using a constant wave amplitude allows us to cover a broader range of relative sizes. Otherwise, to maintain a constant wave steepness, the required wave amplitude would either lower (for large relative size) or higher (for small relative size) than what can be practically generated in the laboratory.

For each size of the sharp-cornered box, three types of simulations are conducted: RANS, Navier–Stokes, and Euler simulations. However, for the round-cornered box, only Navier–Stokes and Euler simulations are considered here. As mentioned before, this is based on the findings by Xiao et al. (2024a), which demonstrate a high level of similarity between the results from RANS and Navier–Stokes simulations for round-corned boxes. Shorthands are used in the figures below to denote different types of simulations: 'SCB-RANS' for RANS simulations of sharp-cornered boxes, 'SCB-Navier–Stokes' for Navier–Stokes simulations of sharp-cornered boxes, 'SCB-Euler' for Euler simulations of sharp-cornered boxes, and similarly for round cornered boxes ('RCB'). The 'RCB' simulations are from Xiao et al. (2024a) and used for comparison.

To better explain the difference in the flow field, pressure distribution, and resultant forces, which result in a difference in drift velocity, simulations for stationary objects were performed. This analysis was specifically carried out for the largest objects (i.e., $l/\lambda = 10\%$). Simulations of stationary objects allow a clearer definition of the relative velocity between the fluid and the objects and have more distinct flow and vorticity field.

We will start our analysis with the motion and drift behaviour of moving objects in Section 3.1, followed by the flow field, pressure distribution and forces for stationary objects in Section 3.2.

3.1. Analysis of moving objects

We first address the drift of moving objects. To ensure that the mesh resolution across all cases is sufficiently fine to accommodate a wall-resolved turbulent model, it is essential to maintain an average y^+ value below 1 throughout the entire simulation duration. Table 4 lists the average y^+ values for simulations of sharp-cornered boxes (both RANS and Navier–Stokes simulations). The mean y^+ value is obtained by first averaging the values across the entire object surface in space and then throughout the simulation in time. As demonstrated in Table 4, the mean y^+ values for all cases remain below 1. Note that the InterDyMFoam uses a dynamic mesh, which can result in significant

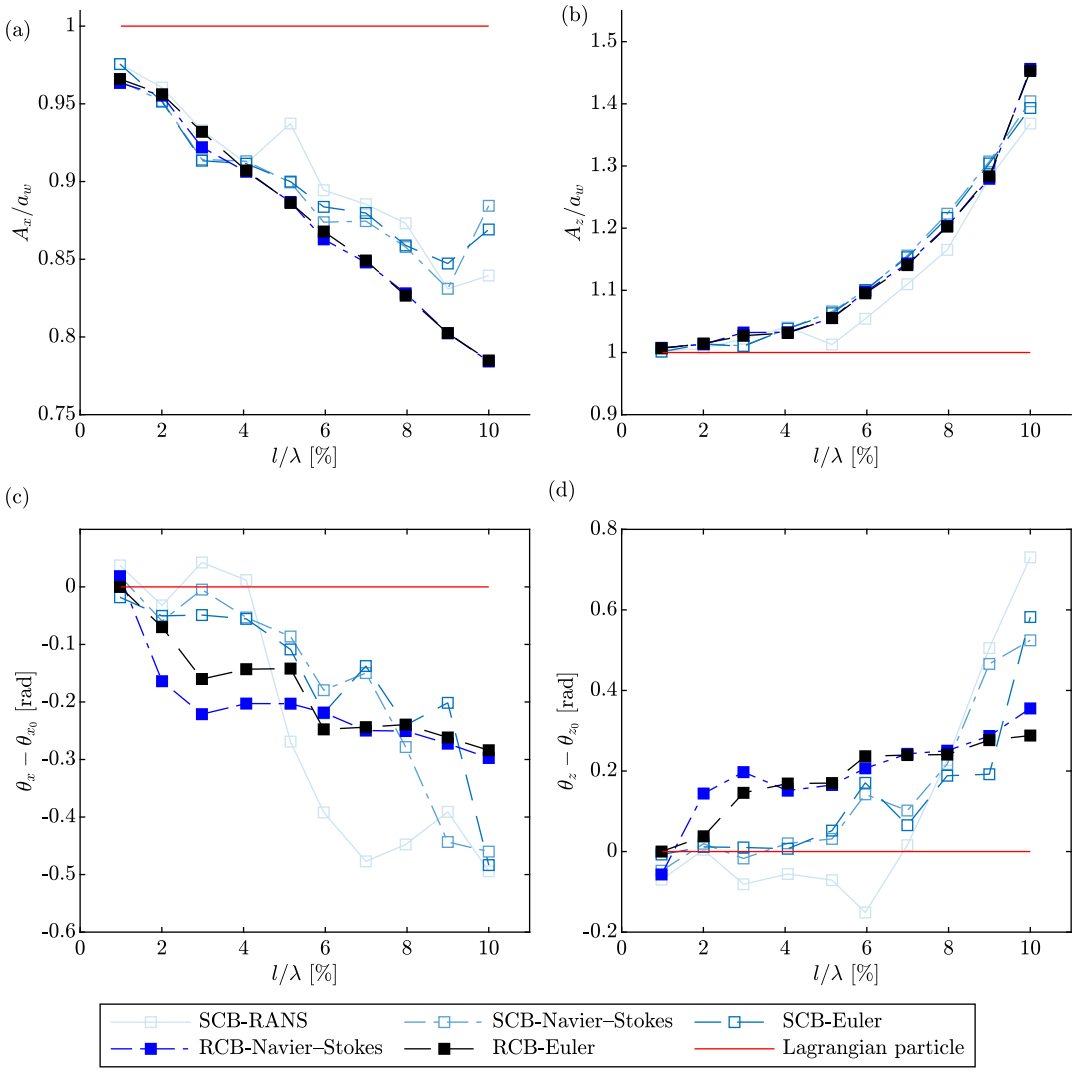

Fig. 3. Oscillatory motion of objects with different corner shapes in different types of simulations in both horizontal and vertical directions: oscillatory motion amplitudes (normalized by input wave amplitude a_w) as a function of relative object size (a) in the horizontal direction A_x/a_w and (b) in the vertical direction A_z/a_w; phase differences of the oscillatory motion between a finite-size object (θ_x, θ_z) and a Lagrangian particle (θ_{x0}, θ_{z0}) with (c) in the horizontal direction ($\theta_x - \theta_{x0}$) and (d) in the vertical direction ($\theta_z - \theta_{z0}$). The red line denotes the results for an ideal Lagrangian particle.

Table 5
Particle Reynolds and Keulegan–Carpenter numbers of moving objects for both round-cornered and sharp-cornered boxes.

	l/λ (%)	1.0	2.0	3.0	4.0	5.0	6.0	7.0	8.0	9.0	10.0
SCB	Re_x	1.80×10^1	2.02×10^2	3.06×10^2	8.52×10^2	1.41×10^3	1.78×10^3	2.78×10^3	3.51×10^3	4.04×10^3	6.96×10^3
	KC	0.24	0.24	0.22	0.24	0.26	0.27	0.30	0.32	0.35	0.38
RCB	Re_x	6.0	2.31×10^2	4.70×10^2	7.63×10^2	1.18×10^3	1.75×10^3	2.31×10^3	2.83×10^3	3.38×10^3	3.85×10^3
	KC	0.27	0.24	0.24	0.24	0.25	0.26	0.28	0.30	0.33	0.36

mesh deformation and distortion when large displacement happens. However, in the cases evaluated here, the displacement (drift) over the duration is not substantial, allowing the solver to maintain accuracy and convergence as the object moves. The particle Reynolds number and Keulegan–Carpenter numbers for both types of objects are given in Table 5. As suggested in the table, the particle Reynolds number falls within the range of $5 < Re_x < 3 \times 10^5$ and the KC numbers satisfy $0 < KC < 0.4$. Because there is limited literature on flow regimes around square cylinders in oscillatory flow with a free surface (cf. Tong et al. (2017)), we use the flow regimes around a circular cylinder in steady current to identify current flow regime. Most of our simulations fall within the subcritical region, where $300 < Re_x < 3 \times 10^5$. This suggests laminar boundary layer separation with a turbulent wake. Regarding the KC number, according to Sumer et al. (2006), Yoon et al. (2016) and Mohseni et al. (2018), when $KC < 3$, the flow is inertia-dominated and the effects of boundary layer separation and vorticity are small. Although vortex formation and a wake structure are observed around the object in our simulations of sharp-cornered boxes, no distinct flow separation has been found to occur.

3.1.1. Object motion and drift

The simulation results are shown in Figs. 3 and 4. Fig. 3 shows the linear oscillatory motions, encompassing both motion amplitudes and phases in both horizontal and vertical directions. The amplitudes and phases of these oscillatory motions are determined by evaluating the phase and magnitude of the linear components only, filtering out sub- and super-harmonics components after the quasi-steady state has been achieved. Fig. 4(a) illustrates the celerity-normalized drift velocity for

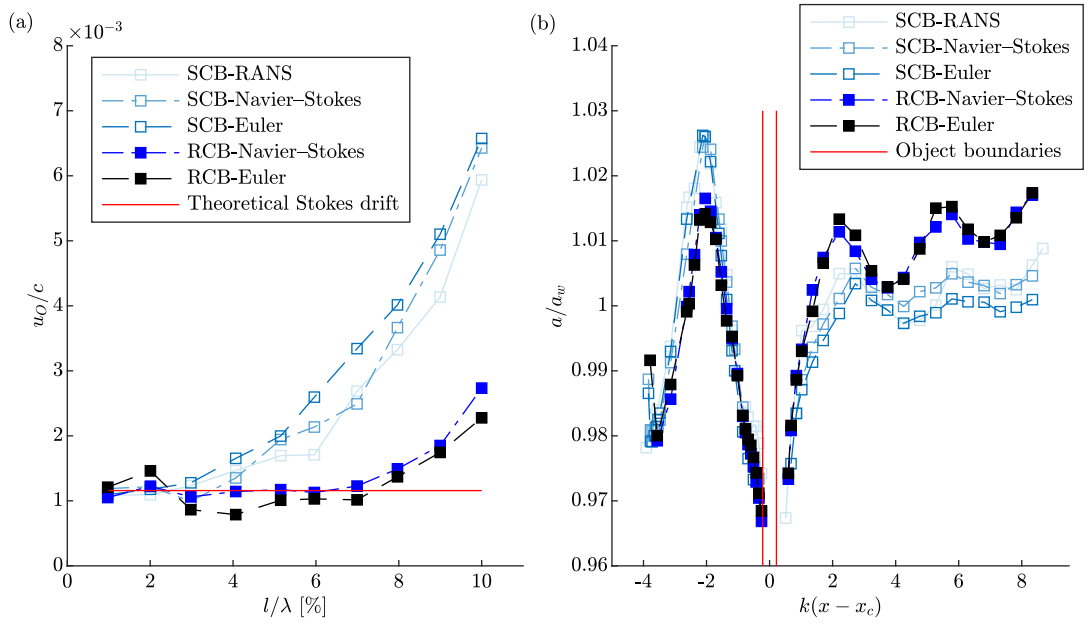

Fig. 4. Drift and local surface elevation for different types of simulations for objects with different corner shapes: (a) celerity-normalized drift velocity u_O/c as a function of relative object size; (b) amplitude of the local surface elevation $a(x)$ (normalized by incoming wave amplitude a_w) as a function of horizontal distance (scaled by wavenumber) from the centre of mass x_c (i.e., standing wave pattern) for an object with relative size $l/\lambda = 7\%$. The object boundaries represent the left and right sides of the objects.

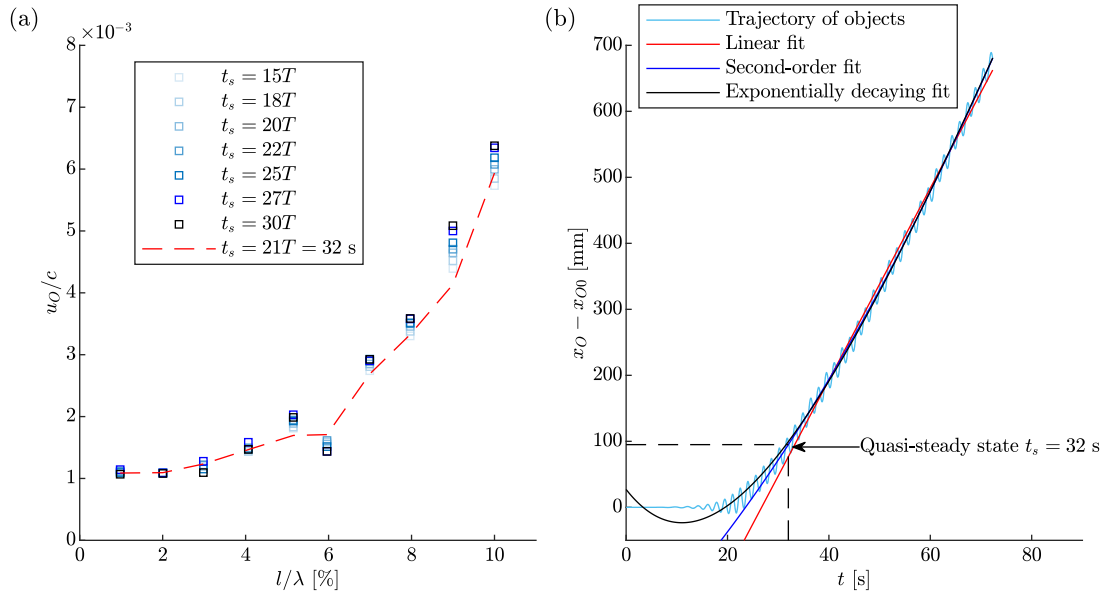

Fig. 5. Examining unsteadiness of the drift velocity of sharp-cornered objects: (a) dependence of drift velocity on the assumed start of the quasi-steady state t_s as a function of object relative size for the RANS simulations. For each relative size, seven different values of t_s are shown, ranging from 23 s to 45 s (i.e., $15T$ to $30T$). The red lines are the drift reported in Fig. 4(a) using $t_s = 21T$; (b) an illustrative example showcasing different types of fits of the horizontal trajectory from the RANS simulations for $l/\lambda = 10\%$. Here, x_O denotes the horizontal position of the object at time t, with $x_{O,0}$ representing the initial position at $t = 0$ s. The red line denotes the linear fit: $x_{O,LF}(t) = 14.5t - 388.4$ (the approach used in Section 3.1.1); the blue line corresponds to the second-order fit: $x_{O,SF} = 0.067t^2 + 7.5t + 214.3$, while the exponentially decaying fit is represented by $x_{O,EF} = 740.1e^{-0.0385t} + 18.64t + 710$. The Stokes drift in this case is $u_S = 2.78$ mm/s. Both linear and second-order fits use the trajectory data after $t_s = 32$ s, whereas the exponential decay fit uses all the trajectory data including from before $t = 32$ s.

all simulation types. Across all cases, a time of $t_s = 21T$ is employed to define the quasi-steady state, where T is the wave period. Fig. 4(b) displays the standing wave pattern as defined in Xiao et al. (2024a) for different simulation types and for sharp-cornered and round-cornered boxes with a relative size of $l/\lambda = 7\%$. The standing wave pattern depicts the local wave amplitude at different locations around the object. The local wave amplitude is obtained by time averaging the magnitude of the surface elevation at specific locations after achieving a quasi-steady state. The surface wave elevation is measured using virtual wave probes in the earth-fixed coordinates system.

Oscillatory motion: To examine the effects of corner shape on object motions, we analyse the amplitudes of oscillatory motions as depicted in Fig. 3(a). Consistent with findings by Xiao et al. (2024a), it is observed that as the object size increases, the amplitudes of horizontal oscillatory motion decrease, while those of vertical oscillatory motion increase. Notably, for relatively large objects, sharp-cornered boxes demonstrate a slightly smaller reduction in horizontal motion amplitude compared to round-cornered boxes. However, the amplitudes of vertical motion for both types of objects are very similar for all relative sizes studied. For sharp-cornered boxes, a comparison between

the 'SCB-Navier–Stokes' and 'SCB-Euler' reveals that the inclusion of viscosity leads to negligible differences in both horizontal and vertical motion amplitudes.

In Fig. 3(c) and (d), a phase lead in the horizontal direction and a phase lag in the vertical direction are observed, qualitatively consistent with the findings of Xiao et al. (2024a). Comparison between the two types of objects reveals that when the object size is small, the sharp corners of the objects exhibit less phase difference in both directions, while larger phase differences are observed for large objects. Furthermore, comparing 'RCB-Navier–Stokes' and 'RCB-Euler' shows that the inclusion of viscosity causes a slightly greater phase lead in the horizontal direction and a greater phase lag in the vertical direction for round-cornered boxes. Conversely, for sharp-cornered boxes, the inclusion of viscosity (that is 'SCB-Navier–Stokes' vs. 'SCB-Euler') does not significantly affect the phase differences in both directions. However, in contrast to 'SCB-Navier–Stokes' and 'SCB-Euler', the 'SCB-RANS' simulations exhibit a non-monotonic trend as the object size increases. This can be explained by the fact that the inclusion of the turbulent viscosity alters the object motion phase in a slightly different way as the object becomes larger.

Overall, the linear motion and phases of the objects in both directions do not exhibit significant differences between objects with different corner shapes and between the different types of simulations.

Object drift and standing wave pattern: we move on to the examine drift velocity in Fig. 4(a). For both types of objects, small objects have a drift equal to the Stokes drift, while larger objects exhibit enhanced drift compared to the theoretical Stokes drift, and such drift enhancement increases with object size, as observed and reported by Xiao et al. (2024a). However, a notable difference is observed between sharp-cornered and round-cornered boxes. The enhanced drift for round-cornered boxes becomes distinct when the object is $l/\lambda \geq 8\%$, whereas the drift enhancement for sharp-cornered boxes is noticeable for objects as small as $l/\lambda = 4\%$. Moreover, the drift enhancement for sharp-cornered boxes is larger. The inclusion of viscosity increases the drift enhancement for round-cornered boxes, while decreasing the drift enhancement for sharp-cornered boxes, suggesting an additional role played by viscosity in the case of sharp-cornered boxes due to their different corner shapes. The inclusion of a turbulence model further reduces the drift enhancement for sharp-cornered boxes by a small amount ('SCB-RANS').

In Fig. 4(b), the standing wave patterns for the different types of simulations and objects are reported. The inclusion of viscosity ('Navier–Stokes' or 'RANS') does not have an obvious influence on the standing wave pattern. However, sharp-cornered boxes experience a more distinct standing wave pattern with a larger local maximum on the upstream side and a smaller local minimum on the downstream side. According to Xiao et al. (2024a), the standing wave pattern is related to diffraction, which results in drift enhancement. The more capable the object is to 'impede' the wave field (i.e., the less streamlined the object is), the more its drift will be enhanced. Therefore, the difference in drift enhancement between two types of objects can partly be explained by the different standing wave patterns.

Given that a standing wave pattern with a local maximum of $a/a_w = 1.12$ in Xiao et al. (2024a) results in a 92% increase in drift relative to standard Stokes drift, the amplitude difference between the standing wave patterns (with a local maximum $a/a_w = 1.026$ for sharp-cornered box vs. $a/a_w = 1.017$ for round-cornered boxes) between the two types of objects is not sufficient to explain the 176% increase in drift of sharp-cornered boxes relative to round-cornered boxes with a relative size of $l/\lambda = 7\%$. The phase difference of linear motion in Fig. 3 may induce small differences in drift enhancement between the two types of objects according to Calvert et al. (2021) and Xiao et al. (2024a), but there must be another explanation to what we observe here.

3.1.2. Drift unsteadiness

Motivated by the difference in drift enhancement between the two types of objects, we revisit the object's trajectory to examine the drift velocity. Previous research, including studies by Nath (1978), Huang et al. (2011), Calvert et al. (2021) and Xiao et al. (2024a), has evaluated drift velocity from drift trajectories using a linear-fit approach after a quasi-steady has been achieved, based on the assumption of steady drift. This same approach is applied in Section 3.1.1. However, in this section, we re-evaluate the drift trajectory of the objects and examine whether it is indeed steady. In Section 3.1.1, we investigated the drift by removing data before the start of the quasi-steady state t_s and performing a linear fit to its horizontal trajectory. Here, we begin by testing the sensitivity of the drift evaluated for different t_s values, using RANS simulations of sharp-cornered boxes, as shown in Fig. 5 (a). The drift velocity shows little dependence on t_s for smaller objects, while varying more for larger objects. This dependence could arise because larger objects have a greater mass and require more time to achieve steady state. Nevertheless, the variations in drift velocity are considered small relative to the drift and drift enhancement. Hence, it is reasonable to conclude that $t_s = 21T$ is an appropriate value for both types of objects. The steady state not having been reached, therefore, cannot account for the difference in drift enhancement between the two object types.

Next, we explore the linear fit approach. A sample trajectory for $l/\lambda = 10\%$ obtained from RANS simulation is presented in Fig. 5(b). Upon closer examination, it becomes apparent that the trajectory may contain other components of behaviour besides the oscillatory component and the constant drift. To examine this further, we perform three types of fits to the object drift trajectory in our data: a linear fit (LF), a second-order fit (SF) and an exponentially decaying fit (EF). The fitting functions are as follows:

$$x_{O,LF}(t) = u_{O,LF}t + d_{LF}, \tag{1}$$

$$x_{O,SF}(t) = s_{O,SF}t^2 + u_{O,SF}t + d_{SF}, \tag{2}$$

$$x_{O,EF}(t) = e_{O,EF}e^{-b_{O,EF}t} + u_{O,EF}t + d_{EF}. \tag{3}$$

All of the fits are performed after filtering out the linear oscillatory part of the motion, retaining only the drift. The linear fit assumes that the object moves steadily with a constant drift. On the other hand, the second-order fit describes an accelerating motion, incorporating both linear and quadratic terms in time. In contrast, the exponential decay fit characterizes the drift motion as a combination of a constant linear drift speed and a transient component that decays exponentially with time. It is evident from Fig. 5(b) that the linear fit does not provide the best fit for the trajectory, particularly for later times.

To quantify the level of unsteadiness in object motion, we introduce the ratio

$$R_a = \left|1 - \frac{u_{O,SF}}{u_{O,LF}}\right|, \tag{4}$$

which measures the relative magnitude of the linear speed in the second-order fit to the (constant) linear speed in the linear fit. The more R_a deviates from 0, the more unsteady the object drift is (typically, $u_{O,SF}/u_{O,LF}$ is smaller than 1, and the larger the ratio R_a is, the more unsteady the drift is). The value of the unsteadiness ratio R_a for both types of objects and the different simulations is illustrated in Fig. 6(a). Additionally, the acceleration $\overline{a}_O$ in Fig. 6(b) represents the mean (time-averaged) value of the acceleration obtained from the motion in the horizontal direction in our simulations, which is evaluated with the oscillatory part not included.

From Fig. 6(a), it is clear that the unsteadiness ratios of both types of objects and simulations are very close to 0 for smaller objects. For round-cornered objects of $l/\lambda \geq 7\%$, there is some unsteadiness, whereas for sharp-cornered objects with relative size $l/\lambda \geq 4\%$, the

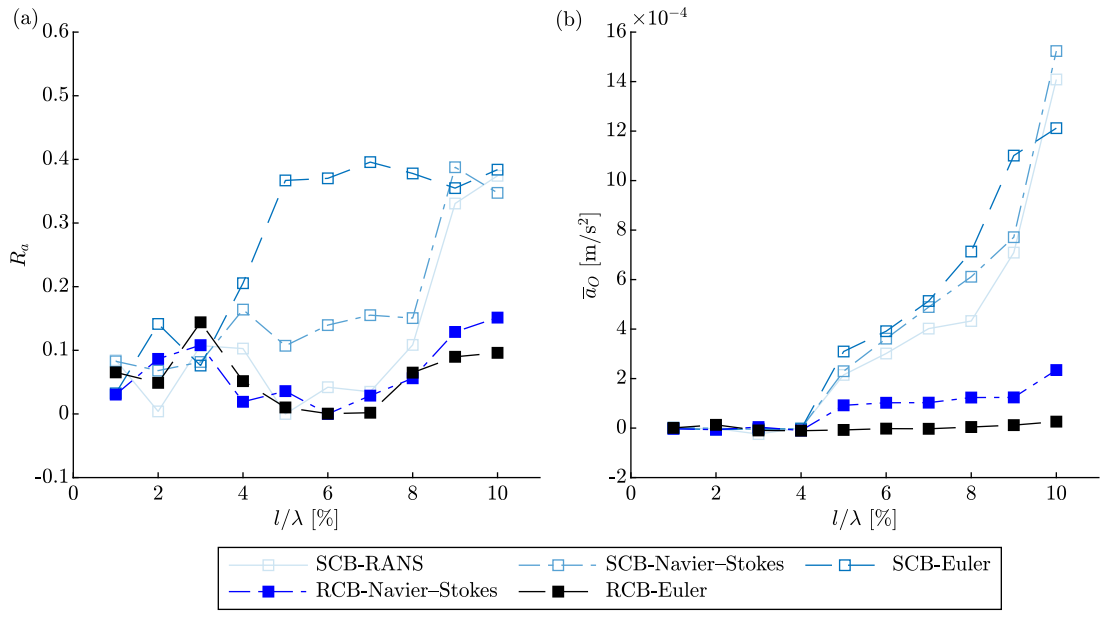

Fig. 6. Unsteadiness of drift for the different object and simulations types: (a) the unsteadiness ratio R_a (b) the mean object drift acceleration ($\overline{a}_O$) as a function of relative size for objects with different corner shapes.

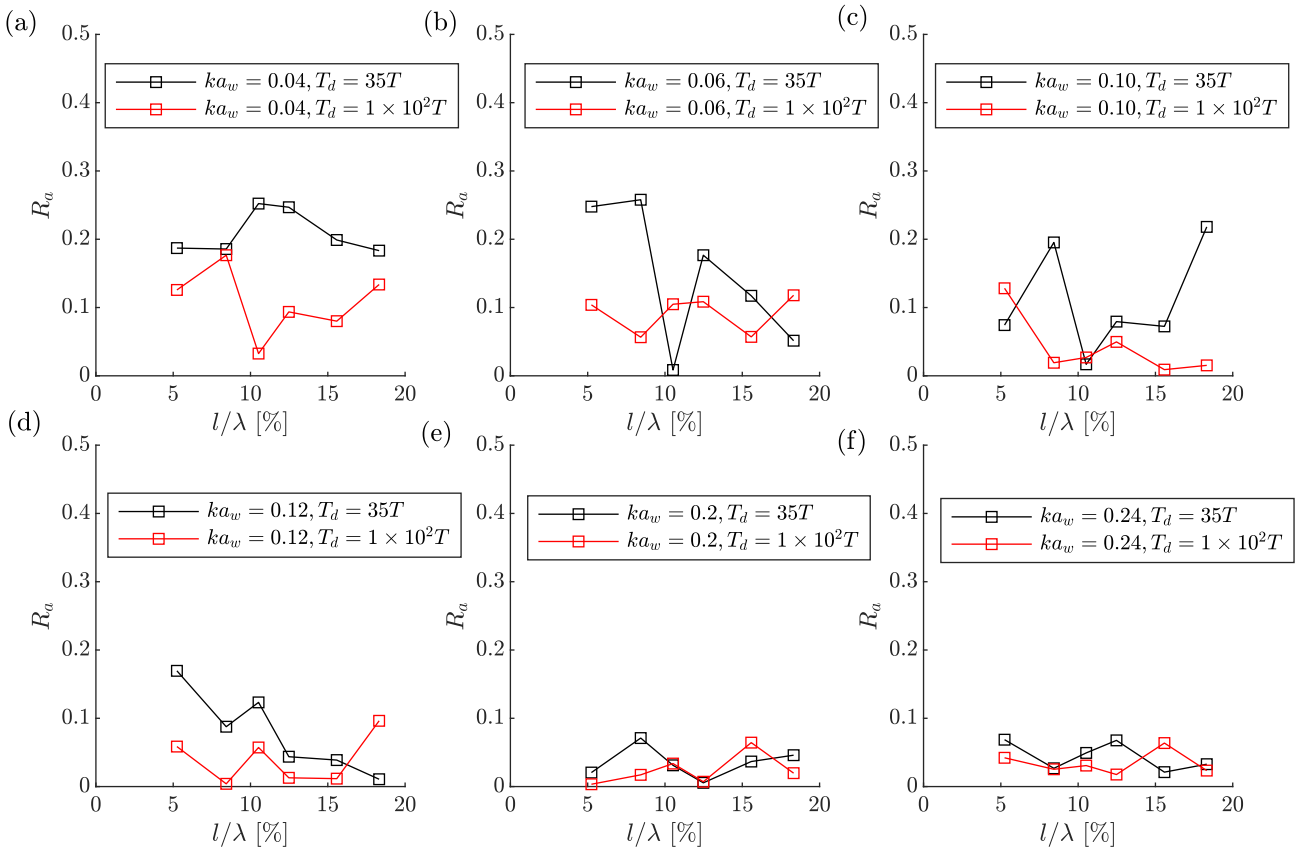

Fig. 7. Unsteadiness ratio of measured drift in the laboratory experiment of Xiao et al. (2024b) as a function of relative object size for different wave steepness values ranging from $ka_w = 0.04$ to $ka_w = 0.24$. The unsteadiness ratio is evaluated from the experimental data for both shorter (black) and longer (red) time durations T_d.

unsteadiness ratio becomes notably larger compared to round-cornered boxes. The comparison between the unsteadiness for different types of simulations for sharp-cornered boxes shows that the 'SCB-Euler' simulation is the most unsteady followed by the 'SCB-Navier–Stokes' and the 'SCB-RANS' simulations. The same trend is observed for the drift velocity observations, where the 'SCB-Euler' simulations demonstrate the largest drift enhancement, followed by the 'SCB-Navier–Stokes' and the 'SCB-RANS' simulations. This might be because the inclusion of viscosity ('SCB-Navier–Stokes' and 'SCB-RANS') helps to suppress the unsteadiness of the drift, showing less drift enhancement. Complementary to this, Fig. 6(b) shows that the average acceleration of sharp-cornered boxes is significantly larger than that of round-cornered

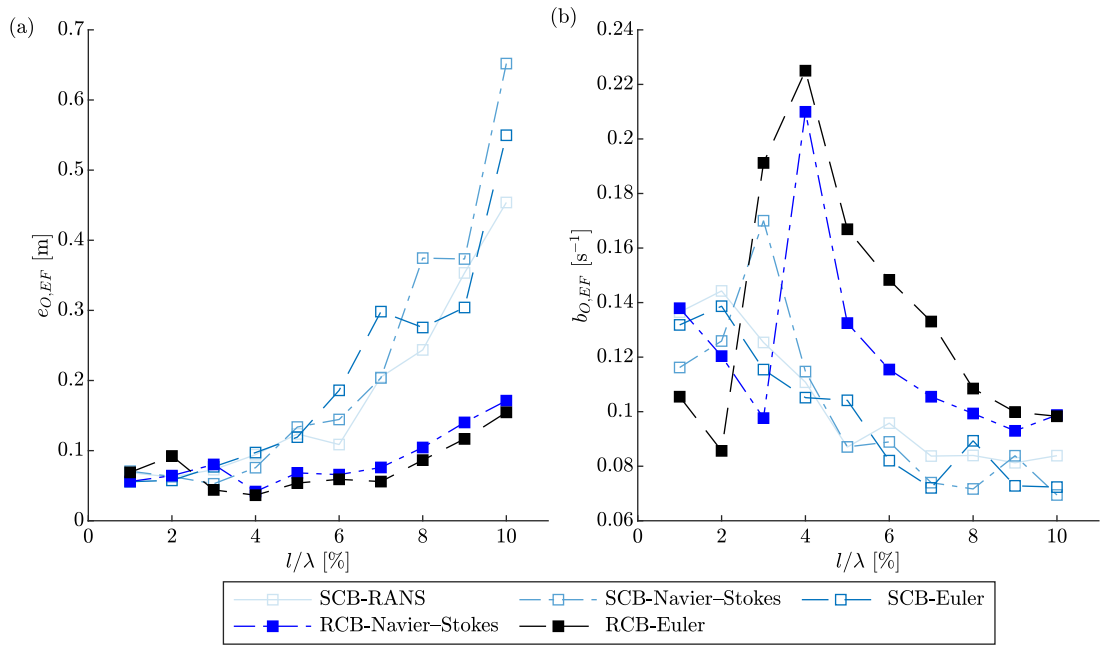

Fig. 8. Parameters of the decaying component of the exponential-decay fit based on (3) as a function of relative size for objects with different corner shapes in different types of simulations: (a) magnitude of the decaying term $e_{O.EF}$, (b) decay rate $b_{O.EF}$.

boxes. For round-cornered boxes, the average acceleration of 'RCB-Euler' is close to 0, and the inclusion of viscosity slightly increases the accelerations. However, for sharp-cornered boxes, the acceleration in the Euler simulations is the largest, and the inclusion of viscosity ('SCB-Navier–Stokes' and 'SCB-RANS') reduces the accelerations (except for the largest object).

Analysis of Fig. 6 suggests that compared to round-cornered boxes, sharp-cornered boxes with equivalent size experience more unsteadiness (acceleration) at a relatively small size on the time scale of the simulations (around $60T$). The unsteadiness can be attributed to two effects: a fundamental unsteadiness and instability induced by the sharp gradients of geometry that will not decay over time, or an initial transient due to the stationary condition of the object at the start of the simulations. To examine the dependence of unsteadiness on the time scale and confirm the underlying reasons for unsteadiness, we have re-evaluated the experimental trajectory data collected by Xiao et al. (2024b), as shown in Fig. 7. It is worth noting that the objects used in the laboratory experiments in their experiment are boxes with sharp corners, and vorticity is reported to have been observed visually for large objects in Xiao et al. (2024b).

To analyse the experimental trajectory data, we use two different time durations, namely a shorter duration of $35T$ and a longer time duration of between 1×10^2T and 1×10^4T to evaluate the unsteadiness of object drift. The shorter duration is consistent with the time duration used in our numerical simulations, while the longer duration corresponds to the duration in the experiments of Xiao et al. (2024b). This longer duration can range between 1×10^2T for the largest objects in high wave steepness and 10^4T for the smallest objects. Fig. 7 shows that for high wave steepness, the unsteadiness ratio shows little dependence on time duration and remains close to 0, suggesting the absence of unsteadiness. For all values of wave steepness, the unsteadiness ratio for the longer duration remains consistently close to 0, regardless of object sizes, whereas similar behaviour is not observed for the shorter duration. Particular attention is paid to the case $ka_w = 0.04$, as this is the wave steepness closest to our numerical simulations. For objects smaller than $l/\lambda = 10\%$, the unsteadiness ratio for the shorter duration is smaller than for the longer duration, suggesting that in low-wave-steepness scenarios, initial transients that ultimately decay may play a role in our relatively short-duration simulations ($T_d = 35T$).

Building on the above analysis of the unsteadiness of the experimental results of Xiao et al. (2024b), we return to our numerical simulations and perform exponentially decaying fits using (3), which are designed to be able to remove initial transients. Instead of allowing for acceleration, we aim to divide the data into two components: one with a constant drift and the other decaying with time. It is found that exponential decay fitting yields better results, as shown in Fig. 5(b). As the parameters of the constant-speed components in (3) are similar to the drift speed shown in Fig. 4(a), only the terms of the exponentially decaying components $e_{O,EF}$ and $b_{O,EF}$ are presented in Fig. 8. The parameter $e_{O,EF}$ determines the magnitude of the exponentially decaying component, and $b_{O.EF}$ denotes its decay rate. The exponential-decay fit is obtained from the entire time history, including $t \le t_s$.

We examine the two parameters in turn, commencing with $e_{O,EF}$. The exponentially decaying component increases with object size, potentially explained by the fact that as the object size grows larger, it gains more mass and thus exhibits greater inertia. The comparison between the two types of object reveals that sharp-cornered boxes contain larger exponentially decaying components, and the size of this component is influenced by the simulation type. For round-cornered boxes, the inclusion of viscosity enlarges the decaying component, while for sharp-cornered boxes, the inclusion of viscosity ('SCB-Navier–Stokes' and 'SCB-RANS') generally reduces it. Maximum values of the decay rate $b_{O,EF}$ are reached for object sizes around $l/\lambda = 4\%$. The sharp-cornered boxes have a smaller decay rate than the round-cornered boxes. Moreover, the inclusion of viscosity ('SCB-Navier–Stokes' and 'SCB-RANS') also influences the decay rate. This analysis further supports the notion that the initial transient (at least, partially) contributes to the unsteadiness observed in Fig. 6. However, this analysis does not provide a definitive answer what would happen in large-duration simulations.

We now turn our attention to exploring how this unsteadiness correlates with the corner shape of objects. We begin by examining the flow field, the vorticity field and the corresponding pressure field at different time intervals. Due to the complexities involved in tracking the pressure history of moving objects, we opted not to analyse the time history of the pressure distributions.

We plot the vorticity and dynamic pressure fields for both sharp-cornered and round-cornered objects in Figs. 9–12. Vorticity is prominently observed in simulations of sharp-cornered boxes, as shown in

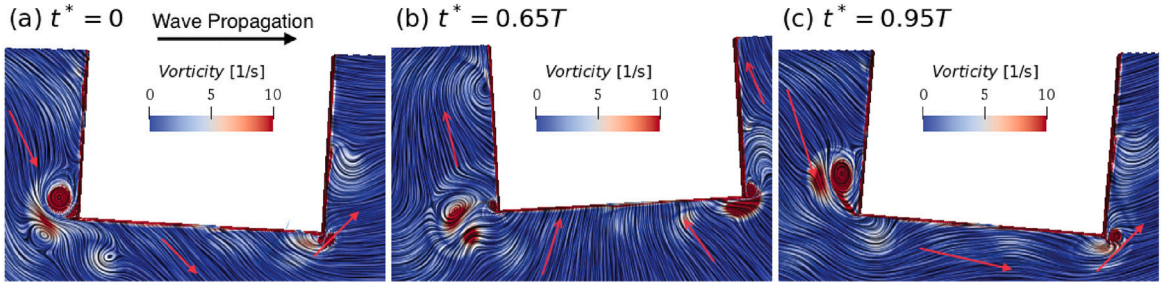

Fig. 9. Vorticity magnitude and flow field (indicated by the streamlines) during one wave period for the RANS simulations of a moving sharp-cornered box ($l/\lambda = 10\%$) for $ka_w = 0.034$. Time starts at $t^* = t - 40$ s (after $t_s = 32$ s) for initial time $t^* = 0$ s, as denoted in the panels. The black arrow indicates the direction of wave propagation, from left to right, while the red arrow shows the approximate flow direction on each side of the object. Note that the object is moving downward in (a), upward in (b) and downward again in (c).

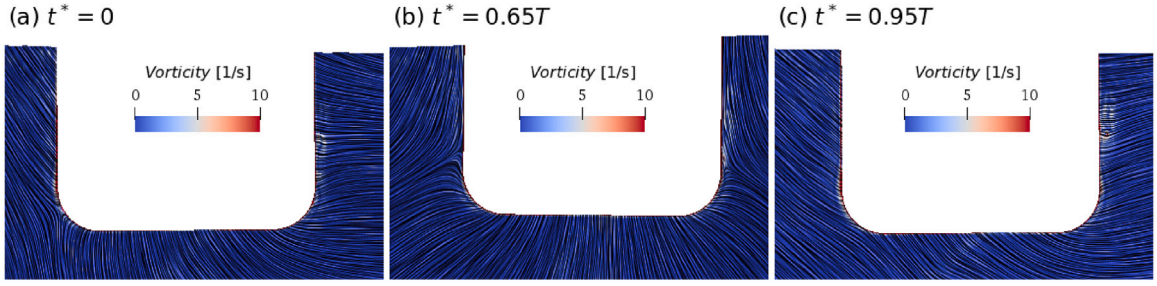

Fig. 10. Vorticity magnitude and flow field (indicated by the streamlines) during one wave period for the Navier–Stokes simulations of a moving round-cornered box ($l/\lambda = 10\%$) for $ka_w = 0.034$. Time starts at $t^* = t - 40$ s (after $t_s = 32$ s) for initial time $t^* = 0$ s, as denoted in the panels.

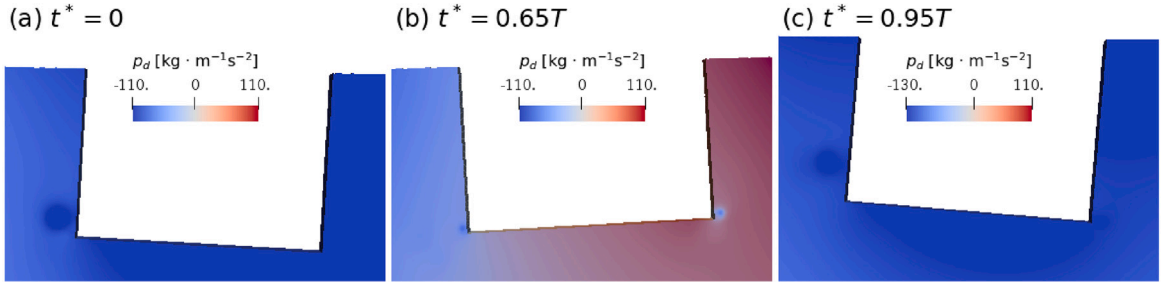

Fig. 11. Dynamic pressure field (p_d) across one wave period for the RANS simulations of a moving sharp-cornered box ($l/\lambda = 10\%$) for $ka_w = 0.034$. Time starts at $t^* = t - 40$ s (after $t_s = 32$ s) for initial time $t^* = 0$ s, as denoted in the panels.

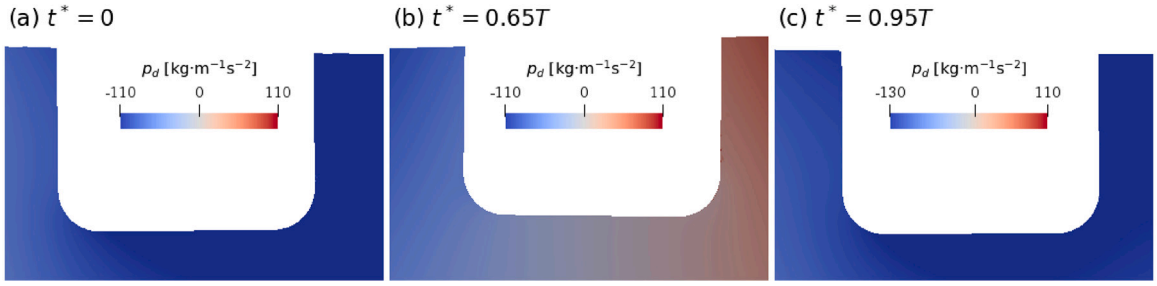

Fig. 12. Dynamic pressure field (p_d) across one wave period for the Navier–Stokes simulations of a moving round-cornered box ($l/\lambda = 10\%$) for $ka_w = 0.034$. Time starts at $t^* = t - 40$ s (after $t_s = 32$ s) for initial time $t^* = 0$ s, as denoted in the panels.

Fig. 9, whereas it is notably absent in simulations involving round-cornered boxes, as shown in Fig. 10. The flow fields, indicated by the streamlines, are also shown in Figs. 9 and 10, where the direction of wave propagation and the flows on each side of the box are also indicated by arrows. The flow directions for the round-cornered objects are not shown in Fig. 10, as they are the same as those depicted in Fig. 9. The presence of vorticity, attributed to the sharp corner, induces changes in the dynamic pressure field around the box, as evident from the comparison between Figs. 11 and 12. Notably, vorticity and flow separation occur unevenly and asymmetrically around the front and rear regions of the sharp-cornered box, as shown in Fig. 9.

Having examined the vorticity and dynamic pressure fields, we proceed to investigate how these factors influence the motions of the object by exploring the different force components experienced by the object. Apart from the gravity and the static pressure force, (both partially and fully) submerged objects exposed to fluid typically experience dynamic

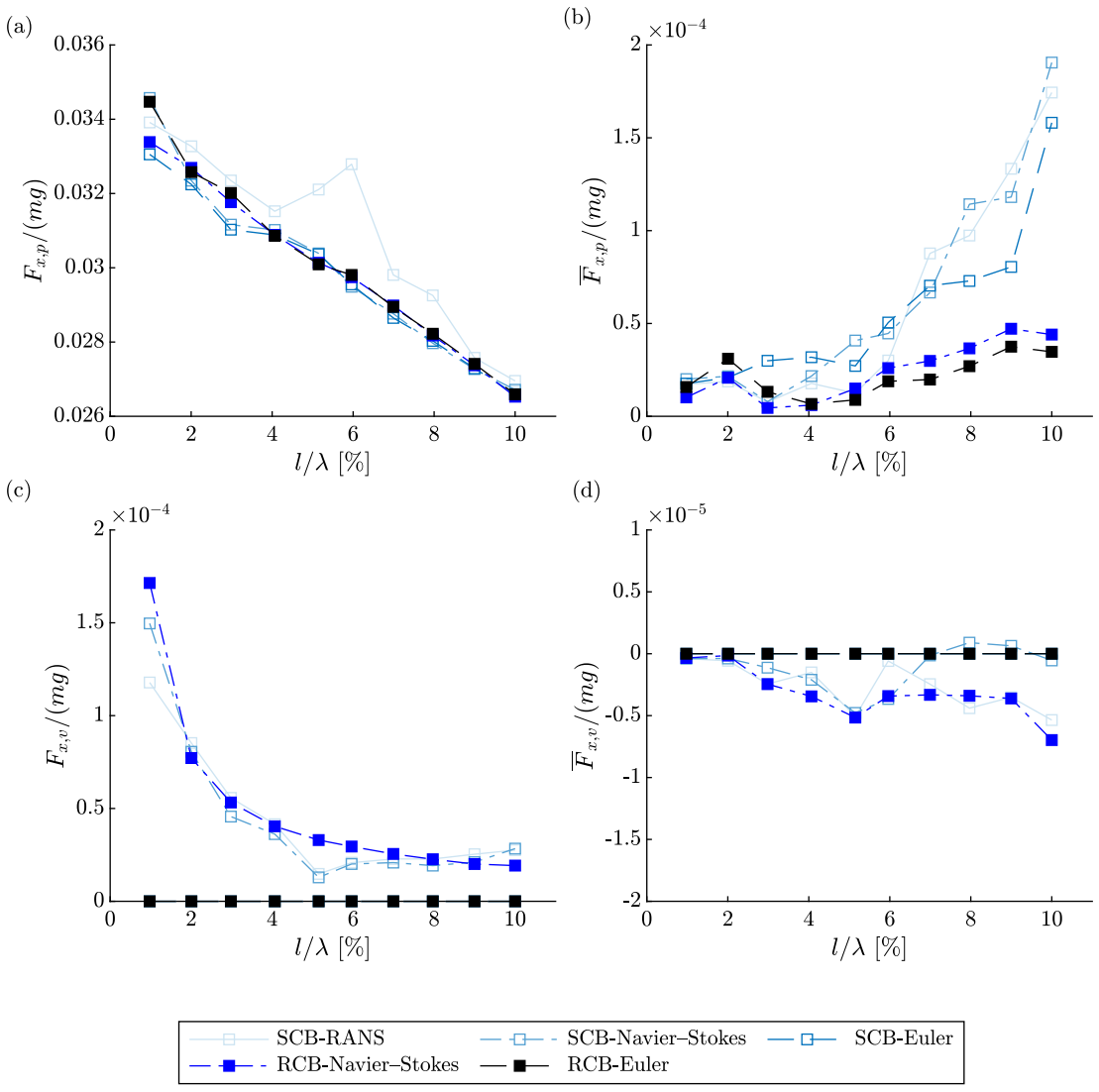

Fig. 13. Magnitudes of the horizontal forces on the object as a function of relative size for objects with different corner shapes in different types of simulations: (a) magnitudes of the oscillatory part of the pressure forces $F_{x,p}$; (b) mean values of the pressure forces $\overline{F}_{x,p}$ over the simulated time duration after $t_s = 21T$; (c) magnitudes of the oscillatory part of viscous forces $F_{v,x}$; (d) mean values of the viscous forces $\overline{F}_{v,x}$ over the simulated time duration after $t_s = 21T$. The forces are all normalized by the gravitational force mg, where m is the mass of the object and $g = 9.81$ m/s^2. For 'SCB-Euler' and 'RCB-Euler', viscous forces are all 0, as viscosity is not included in these simulations.

pressure and viscous forces. In this analysis, we focus on the horizontal direction. Fig. 13 presents the magnitudes and time-averaged values of the dynamic pressure and viscous force components for objects of different sizes and corner shapes and for the different simulation types. Notably, the figure illustrates that pressure forces outweigh viscous forces by two orders of magnitude.

The comparison between two types of objects and the different types of simulations reveals that compared to round-cornered boxes, the magnitude of pressure and viscous forces for sharp-cornered boxes are slightly smaller but the differences are not significant. The inclusion of viscosity does not exert a pronounced influence on the magnitudes of these forces for both types of objects. An exception is observed in the RANS simulations of sharp-cornered boxes, where there appears to be a smaller magnitude of the oscillatory component of the pressure forces compared to other types of simulations, consistent with the oscillatory motions depicted in Fig. 3. However, comparison of mean values reveals significant differences between the two types of objects and different types of simulations. The sharp-cornered boxes experiences larger mean values of pressure forces than the round-cornered boxes. Relating the mean value of the pressure force to the acceleration in Fig. 6(b), we observe consistent trends. Compared to the round-cornered boxes, the larger dynamic pressure forces on the sharp-cornered boxes are likely to be induced by the asymmetry in the vorticity field, which results in net drift forces that accelerate the object forward. The inclusion of viscosity ('SCB-Navier–Stokes' and 'SCB-RANS') plays a role in suppressing or influencing the generation and development of vorticity, subsequently affecting the forces and consequently its drift behaviour. Regarding the mean value of the viscous forces, round-cornered boxes experience the highest values, followed by the RANS and Navier–Stokes simulations of sharp-cornered boxes, suggesting sharp-cornered boxes experiences relatively lower mean viscous force due to the alterations in the fluid field.

To better understand the pattern of vorticity generation over time, especially under oscillatory forcing, it is crucial to explore the relationship between corner shape, vorticity generation, dynamic pressure fields, and resultant forces. However, analysing this relationship for moving objects is challenging due to the constantly changing relative positions between the object and the fluid field, as they oscillate and drift. We therefore conduct additional analysis focusing on stationary objects.

Table 6
Detailed coordinates of the sampling points in the fluid field shown in Fig. 14 for stationary objects for different wave steepness values. The variables x and z represent the horizontal and vertical coordinates of the points, respectively, while x_c is the horizontal coordinates of the centre of object. Variables l and h_d denote the length and draft of the objects, respectively. Consequently, the horizontal locations of lines AB and CD are $x - x_c = -0.5l$ and $x - x_c = 0.5l$, respectively. The vertical locations of lines $A'D'$ and BC are $z/h_d = 0$ and $z/h_d = -1$, respectively. For $ka_w = 0.034$, the sampling points cover the region of $-0.65l \le x - x_c \le 0.57l$ and $-0.12h_d \le z \le -1.2h_d$. For higher wave steepness values $ka_w = 0.07, 0.09$, the region expands to $-0.76l \le x - x_c \le 0.65l$ and $-0.26h_d \le z \le -1.32h_d$.

ka_w	Location	Left region					Bottom region				Right region			
		l_1	l_2	l_3	l_4	l_5	b_1	b_2	b_3	b_4	r_1	r_2	r_3	r_4
0.03		$(x-x_c)/l \in [-0.65, -0.52]$					$(x-x_c)/l \in [-0.46, 0.54]$				$(x-x_c)/l \in [0.52, 0.57]$			
	z/h_d	−0.12	−0.6	−0.72	−0.8	−0.98	−1.04	−1.1	−1.16	−1.2	−0.8	−0.84	−0.92	−0.96
0.07		$(x-x_c)/l \in [-0.76, -0.52]$					$(x-x_c)/l \in [-0.46, 0.54]$				$(x-x_c)/l \in [0.52, 0.65]$			
	z/h_d	−0.26	−0.52	−0.6	−0.8	−0.98	−1.04	−1.16	−1.2	−1.32	−0.26	−0.6	−0.72	−0.98
0.09		$(x-x_c)/l \in [-0.76, -0.52]$					$(x-x_c)/l \in [-0.46, 0.54]$				$(x-x_c)/l \in [0.52, 0.65]$			
	z/h_d	−0.26	−0.52	−0.6	−0.8	−0.98	−1.04	−1.16	−1.2	−1.32	−0.26	−0.6	−0.72	−0.98

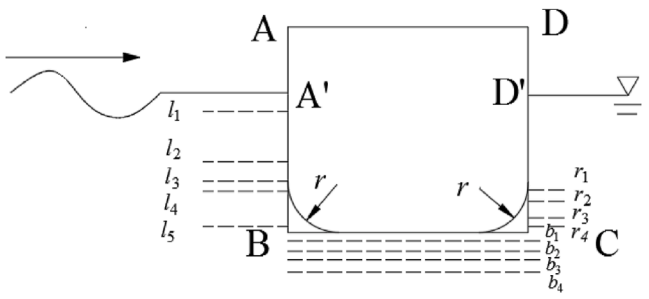

Fig. 14. Diagram of the stationary box with both types of corner shapes and the locations of sampling points in the fluid field around the box for the stationary object simulations. In the diagram, A and D represent two endpoints at the top of the box, while A′ and D′ denote the points of intersection of the box with the still-water level. The sampling points are categorized based on their location (letter) followed by vertical position (number), e.g., l_1. Several points are positioned at the same vertical locations. Typically, for the left and right sides of the region, 5 to 6 points are located on each line while for the bottom region, 8 to 10 points are distributed on each line.

3.2. Analysis of stationary objects

We have conducted simulations of stationary boxes with two corner types, sharp and round, at the largest size, $l/\lambda = 10\%$ for three different wave steepness values: $ka_w = 0.034, 0.07, 0.09$. For sharp-cornered boxes, we conduct RANS, Navier–Stokes and Euler simulations, while for round-cornered boxes, only Navier–Stokes simulations are performed for comparison. As the object is stationary, it is straightforward to set sampling points around the object to collect time–history data for analysis. The sampling points are categorized into two types: points on the object boundaries and points in the surrounding fluid field. For the points on the object boundaries, we evenly distributed 10 points along each edge. Regarding the points in the surrounding fluid field, these are located in the left (front), bottom and right(rear) regions surrounding the objects, as shown in Fig. 14. The detailed coordinates of these points are provided in Table 6. The distribution of points is designed to cover the main regions where the vorticity and flow separation occur. It is noteworthy that as the vorticity generation is not symmetrical on the upstream and downstream sides, we also distribute the sampling points asymmetrically. Specifically, for the left region, our sampling points span $0.13l$, while for the right side, only $0.05l$ is considered. The values of y^+ and the relevant non-dimensional numbers for these simulations are given in Appendix C.1. We examine the surface elevation around the stationary objects in Appendix C.2.

3.2.1. Vorticity and dynamic pressure field

Next, we examine the fluid and vorticity fields over one wave cycle. Fig. 15 presents the vorticity magnitude and the flow fields, as indicated by streamlines, over one wave period for the RANS simulations of a stationary object with sharp corners when $t^* = t - 40$ s (which is larger than $t_s = 32$ s). The directions of wave propagation of the flows over each side of the object are also indicated in Fig. 15 by arrows. The flow directions for the round-cornered objects are not shown in Fig. 16, as they are the same as those depicted in Fig. 15. We can see that the vorticity is asymmetrically generated around the two corners. The front (left) experiences larger vorticity, covering a larger area compared to the rear. Additionally, the vorticity pattern appears to be periodic, as evident when comparing panel (a) with panel (f) at $t = 0$ and $t = 0.98T$, respectively. In contrast, Fig. 16 gives the corresponding vorticity and flow field for round-cornered boxes. The streamlines are smooth, with little vorticity, consistent with our findings for moving objects. Spectral analysis of the turbulent kinetic energy for the sampling points in the fluid field is conducted in Appendix C.3.

The corresponding dynamic pressure fields for boxes with sharp-cornered and round-cornered boxes are given in Figs. 17 and 18, respectively. A noticeable difference can be observed in the pressure gradient/distributions at the locations where the vorticity is generated, leading to different pressure forces after integration over the boundaries. We note that similar analyses are conducted for viscid simulations using the Navier–Stokes equations and inviscid simulations using the Euler equations of the sharp-cornered box, revealing larger vorticity magnitude and broader vorticity generation areas in Euler simulations compared to RANS and Navier–Stokes simulations. This subsequently induces different dynamic pressure fields and pressure forces. The inclusion of viscosity helps to suppress the generation of vorticity and reduce its magnitude. However, these results are not presented here for brevity. The trends observed are consistent for higher wave steepness, albeit with larger vorticity magnitudes in larger areas.

To further support and quantify these observations, we analyse dynamic pressure over the object boundaries. The magnitude and time-averaged value of the dynamic pressure for low wave steepness, serving as a representative case, are given in Fig. 19 where the magnitude (of the oscillatory part) and the mean value are both evaluated after t_s. The figure shows that the primary difference between the two types of objects occurs on the front edges.

3.2.2. Force analysis

Thus far, we have looked at how the vorticity generated due to the sharp corner alters the dynamic pressure distributions. The analysis proceeds to examine the relationship between dynamic pressure distributions and object motions over time through analysis of the forces, as shown in Fig. 20. Here, both magnitudes and mean values of the pressure and viscous forces are compared. It is shown that sharp-cornered boxes exhibit larger magnitudes of the oscillatory components and larger mean values of pressure forces relative to round-cornered boxes for all wave steepness explored here, aligning with the observations from Fig. 19. Conversely, the forces for round-cornered boxes have larger viscous magnitudes and absolute mean values compared to their sharp-cornered counterparts.

Comparing with those for moving objects in Fig. 13, we see consistent results: for all wave steepness explored here, sharp-cornered boxes experience larger mean values for both pressure forces and viscous

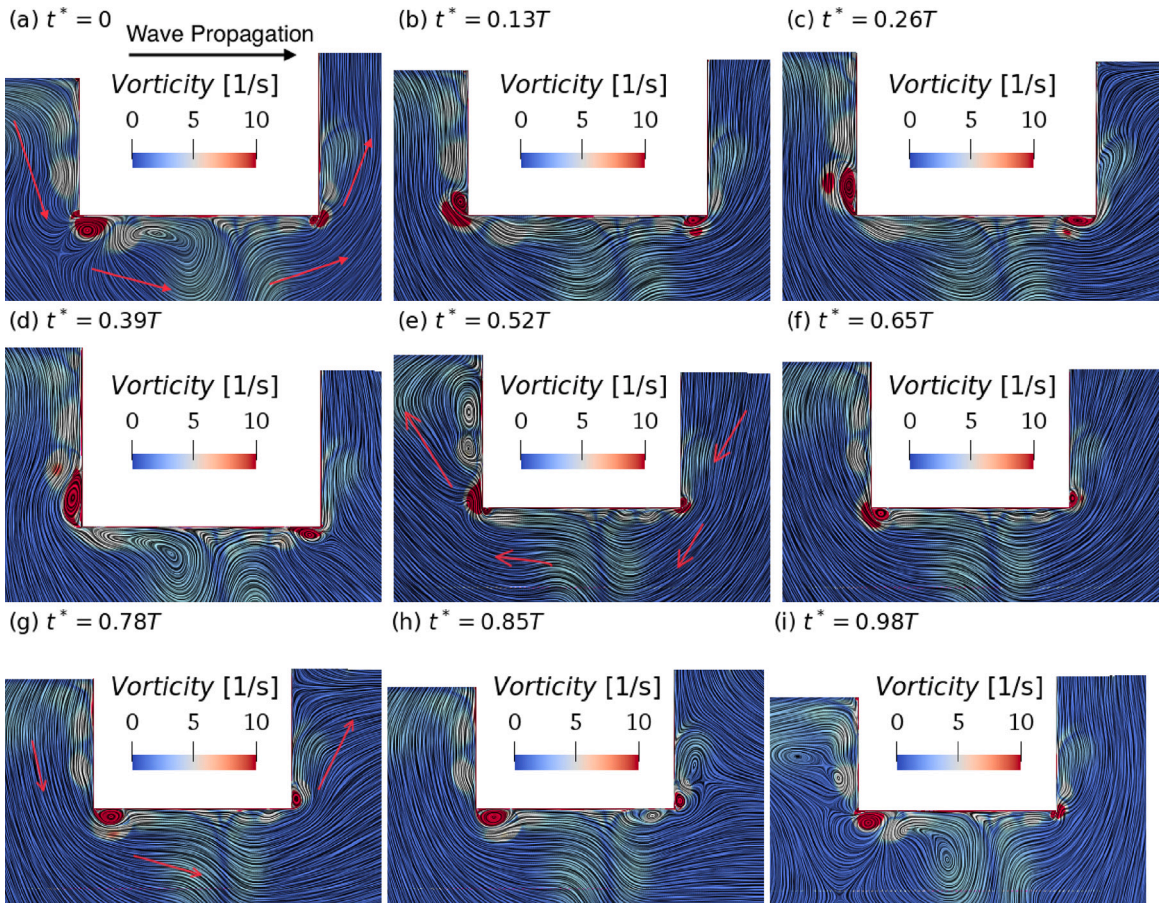

Fig. 15. Vorticity magnitude and flow field (indicated by the streamlines) during one wave period for the RANS simulations of a stationary sharp-cornered box with $l/\lambda = 10\%$ for $ka_w = 0.034$. The black arrow indicates the direction of wave propagation, from the left to right, and the red arrow shows the approximate flow direction on each side of the object.

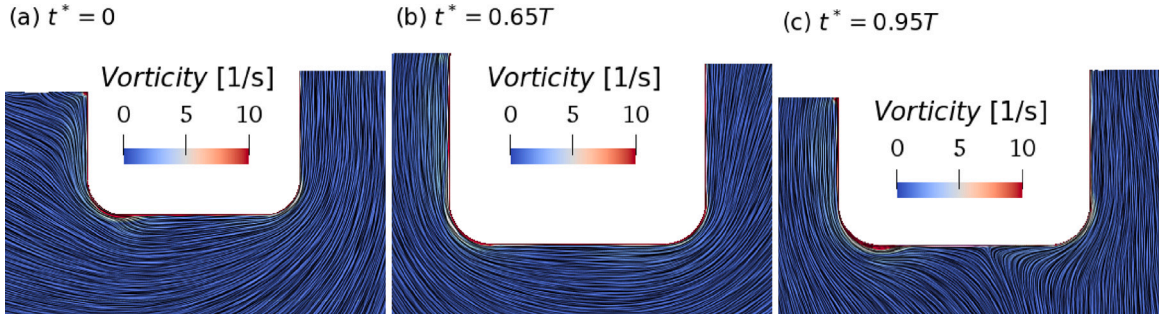

Fig. 16. Vorticity magnitude and flow field (indicated by the streamlines) during one wave period for the Navier–Stokes simulations of a stationary round-cornered box with $l/\lambda = 10\%$ when $ka_w = 0.034$. Time starts at $t^* = t - 40$ s (after $t_s = 32$ s) for initial time $t^* = 0$ s, as denoted in the panels.

forces, as well as larger magnitudes of the oscillatory components of the viscous forces. However, for moving objects, there is no pronounced difference (which is also inconsistent) between the two types of objects regarding the magnitude of the oscillatory pressure forces as shown in Fig. 13(a). For the largest object $l/\lambda = 10\%$, this discrepancy may be attributed to the object's drift motion, which alleviates the impedance and disturbance caused by the objects to the fluid field, thereby mitigating the differences between the two types of objects.

4. Conclusion

This paper has investigated the influence of corner shape on the drift behaviour of bluff-bodied objects (rectangular boxes) floating on unidirectional, deep-water surface gravity waves. This work builds on numerical simulations and experiments by Xiao et al. (2024a,b). Compared to Xiao et al. (2024a,b), the present paper has identified a new mechanism for drift enhancement: the vorticity generated by sharp corners and the pressure distribution this generates. Two different corner shapes have been considered: sharp corners and round corners with a corner radius of up to 24% of the object's draft. Three types of models are used that solve the Reynolds-Averaged Navier–Stokes (RANS), Navier–Stokes (viscid) and Euler equations (inviscid) respectively. We restrict our analysis to objects with sizes less than 10% of the wavelength. The particle Reynolds Re_x and Keulegan–Carpenter (KC) numbers are in the range of $6 < \mathrm{Re}_x < 8 \times 10^4$ and $0 < \mathrm{KC} < 0.9$, suggesting a turbulent wake (with laminar boundary layer separation) and a small amount of flow separation. We observe vortex formation

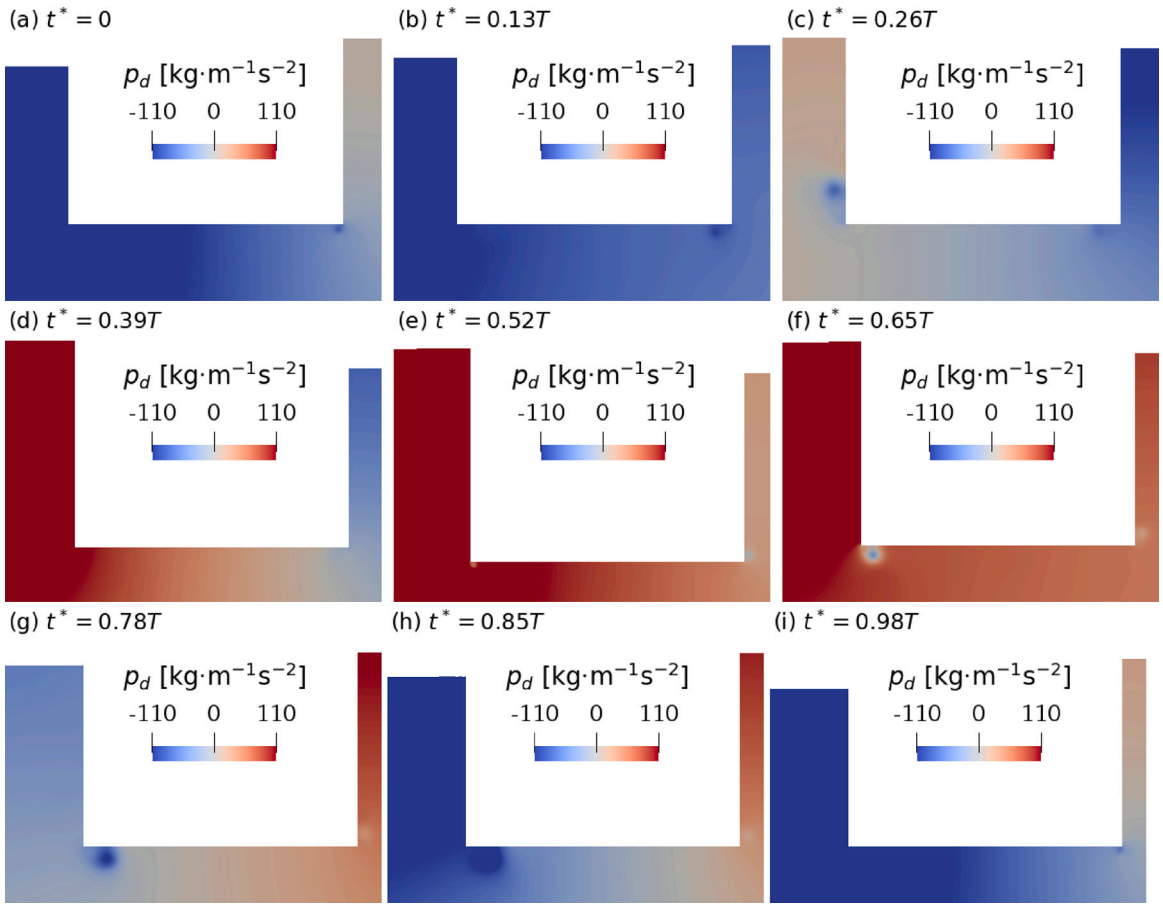

Fig. 17. Dynamic pressure field p_d during one wave period for RANS simulations of a stationary sharp-cornered box with $l/\lambda = 10\%$ when $ka_w = 0.034$. Time starts at $t^* = t - 40$ s (after $t_s = 32$ s) for initial time $t^* = 0$ s, as denoted in the panels.

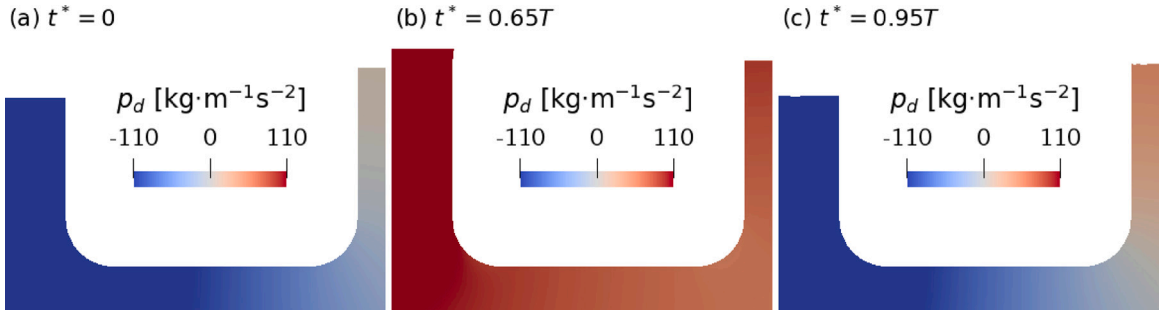

Fig. 18. Dynamic pressure field p_d across one wave period for Navier–Stokes simulations of a stationary round-cornered box with $l/\lambda = 10\%$ when $ka_w = 0.034$. Time starts at $t^* = t - 40$ s (after $t_s = 32$ s) for initial time $t^* = 0$ s, as denoted in the panels.

in the simulations of sharp-cornered boxes which is absent for round-cornered boxes. We observe significantly larger drift enhancement (compared to the theoretical Stokes drift) for objects with sharp corners and show that the drift of these objects becomes unsteady. In addition to previously identified mechanisms of drift enhancement that arise from (viscous) drag (Calvert et al., 2021) and diffraction of the wave field (Xiao et al., 2024a), which together explain only part of the drift enhancement found here, we identify another mechanism related to vortex formation that contributes to the drift enhancement of objects with sharp corners.

Consistent with the findings of Calvert et al. (2021) and Xiao et al. (2024a), we observe that drift enhancement for boxes with both shapes of corners is only relevant for objects larger than a few percent of the wavelength. For smaller objects ($l/\lambda \leq 3\%$ in this study, with l representing the length of the object and λ the wavelength), the non-Lagrangian behaviour is less evident and the drift speed of the objects is equal to the Stokes drift. However, as size increases, a difference in velocity between the object and its surrounding fluid emerges, corresponding to enhanced drift compared to a Lagrangian tracer. Importantly, objects with sharp corners experience much greater drift enhancement than objects of equivalent size with round corners. For instance, compared to a Lagrangian tracer, there is a 454% increase in drift for a sharp-cornered box and a 134% increase for a round-cornered box when $l/\lambda = 10\%$. Furthermore, sharp-cornered boxes experience non-negligible enhanced drift from relatively smaller sizes ($l/\lambda \geq 4\%$) compared to round-cornered boxes ($l/\lambda \geq 7\%$). The presence of vorticity due to the sharp corners results in changes to the dynamic pressure field and subsequently affects the forces exerted on the object. Larger magnitudes of vorticity and vorticity-containing regions on the upstream side of sharp-cornered boxes lead to larger magnitudes of

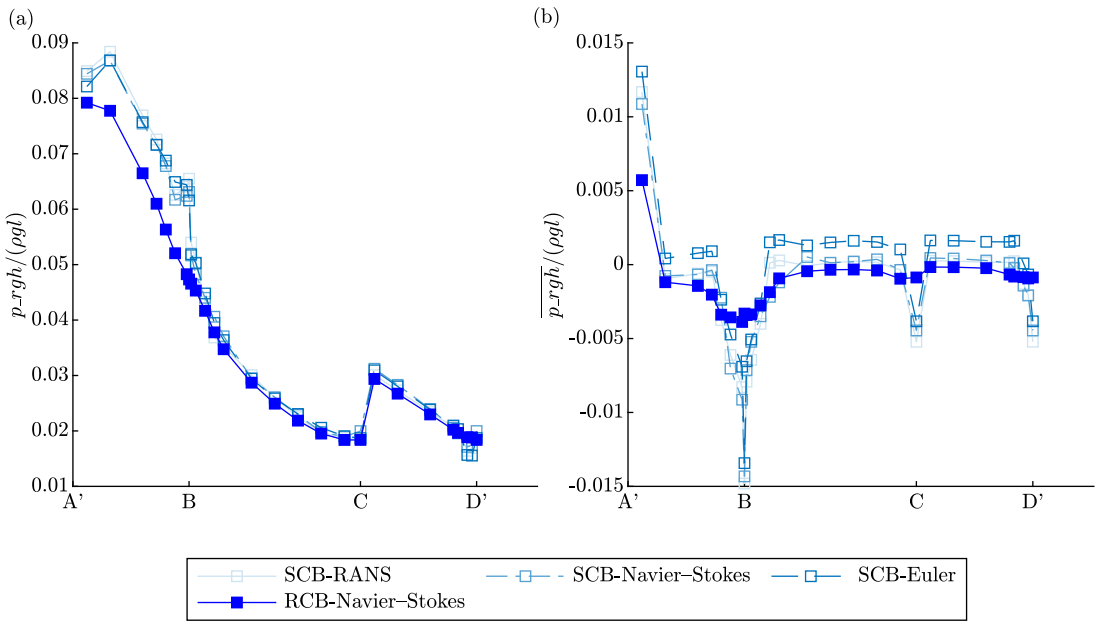

Fig. 19. Dynamic pressure p_rgh (scaled by ρgl) distributions over the object boundaries for objects with $l/\lambda = 10\%$ and two different corner shapes for $ka_w = 0.034$: (a) dynamic pressure magnitude (p_rgh), normalized by ρgl, for different types of simulations; (b) mean values of dynamic pressure $\overline{p\_rgh}$, normalized by ρgl, for different types of simulations.

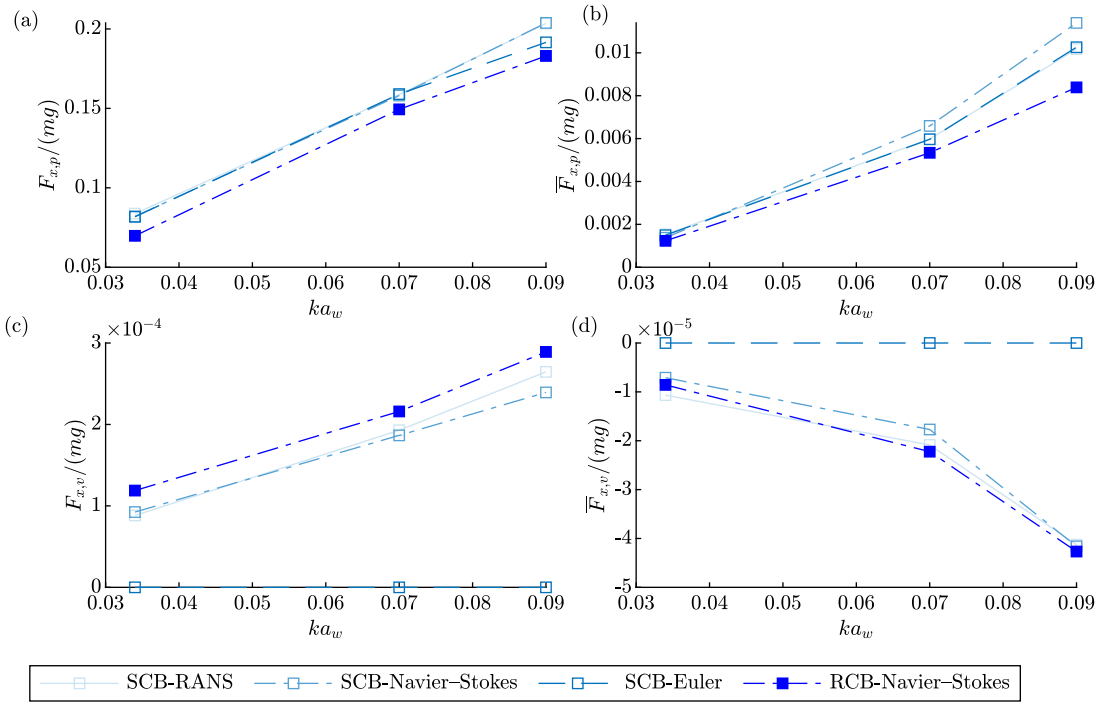

Fig. 20. Horizontal forces as a function of wave steepness for objects with different corner shapes in different types of simulations: (a) magnitudes of the oscillatory part of pressure forces $F_{x,p}$; (b) mean values of pressure forces $\overline{F}_{x,p}$ over the simulated time duration after $t_s = 21T$; (c) magnitudes of the oscillatory part of viscous forces $F_{x,v}$; (d) mean values of viscous forces $\overline{F}_{x,v}$ over the simulated time duration after $t_s = 21T$. Notably, for 'SCB-Euler', viscous forces are all 0 owing to the absence of viscosity in these simulations.

the oscillatory forces (more observable for stationary objects) and mean (time-averaged) forces. Viscosity plays a dual role in object drift. First, viscosity induces a phase difference between the object and the surrounding fluid, which acts to enhance drift, as described by Calvert et al. (2021); this occurs for objects with both sharp and round corners. Second, viscosity suppresses vorticity generation, reducing its magnitude and restraining its development for sharp-cornered boxes, thus mitigating drift enhancement.

Finally, we examine the potential unsteadiness of the drift of objects. Our analysis reveals that objects with sharp corners exhibit greater unsteadiness in their drift compared to round-cornered objects. Evaluating the unsteadiness over different durations using experimental data from Xiao et al. (2024b) suggests that, for low wave steepness, the duration of numerical simulations may not be sufficient for transient behaviour to disappear and for the object to reach a quasi-steady state, indicating that at least part of the unsteadiness will diminish with time and may be the result of an initial transient. However, considering that vorticity is periodically generated by the periodic incoming waves, it is likely that the unsteadiness of drift is fundamental and persists over time. Determining which of the two hypothesis is correct requires

large duration experiments and numerical simulations, and these are recommended as future work.

Although the current numerical simulation uses a model developed by Xiao et al. (2024a), which has been compared to experiments in Xiao et al. (2024b), the capability of the model to predict the drift for both object shapes would benefit from a comparison with experimental for round-cornered objects, which were not considered by Xiao et al. (2024b). Additionally, the vorticity and turbulence in the RANS simulations needs further verification through comparison with Large Eddy Simulations (LES) or Direct Numerical Simulation (DNS).

The present study focuses on the drift of objects with relative sizes l/λ ranging from 1% to 10%, forlimited wave steepness conditions and two corner shapes. Xiao et al. (2024b) reports a critical value of steepness ($ka_w \geq 0.2$ with k representing wavenumber and a_w wave amplitude) and relative size ($l/\lambda \geq 15\%$), where the mechanisms dominating drift enhancement changes. A more systematic exploration of the effect of different relative sizes, corner shapes (e.g., varying round corner radii, chamfered corners) and wave steepness on this transition is needed and recommended as future work.

CRediT authorship contribution statement

Qian Xiao: Writing – original draft, Validation, Methodology, Investigation, Formal analysis, Data curation, Conceptualization. **Shiqiang Yan:** Validation, Software. **Thomas A.A. Adcock:** Writing – review & editing, Supervision. **Ton S. van den Bremer:** Writing – review & editing, Supervision, Conceptualization.

Declaration of Generative AI and AI-assisted technologies in the writing process

During the preparation of this work the author(s) used ChatGPT in order to revise the original draft for checking the grammar, spelling and the vocabulary. After using this tool/service, the author(s) reviewed and edited the content as needed and take(s) full responsibility for the content of the publication.

Declaration of competing interest

The authors declare that they have no known competing financial interests or personal relationships that could have appeared to influence the work reported in this paper.

Acknowledgements

Q.X. is supported by the China Scholarship Council-PAG Oxford Scholarship. T.S.vdB was supported by a Royal Academy of Engineering Research Fellowship.

Appendix A. Convergence study for stationary objects

A convergence study and grid dependency analysis are conducted for objects with sharp corners on the waves with lowest ($ka_w = 0.034$) and highest wave steepness ($ka_w = 0.09$) in our simulations. The convergence study has been conducted for both the InterDyMFoam solver and QaleFEM solver, but only the results of the InterDyMFoam Navier–Stokes solver are presented in this paper, as discretization error is typically the main source of errors in CFD solvers. The meshing in the Navier–Stokes domain is constructed using blockMesh and snappyhexMesh with refinement near the object and the free surface. The aspect ratio of the mesh near the object is set to 1. Near the surface, the addlayer in snappyHexmesh is typically set to 6 or 10, and the surface refinement level is set to 2. RefinewallLayer is used in some cases to further refine the mesh near the wall. The convergence study is carried out for the stationary object with the largest objects of size $l/\lambda = 10\%$ (λ is the wavelength), subjected to waves with the low wave steepness $ka_w = 0.034$ as well as the highest wave steepness $ka_w = 0.09$ where k is the wave number and a_w is the wave amplitude. We include low wave steepness because it represents the main wave steepness in our later explorations. The object has length $l = 0.037$ m, height $h = 0.055$ m, draft $h_d = 0.025$ m, and density $\rho = 781$ kg/m^3. We perform this convergence study for stationary objects. When the object is stationary, the relative velocity between the object and the flow is larger and the flow is more turbulent than for the moving objects (both particle Reynolds number Re_x and Keulegan–Carpenter number KC are therefore higher). That is to say, for stationary cases, it is more challenging to achieve convergence.

We use three sets of refinements: Mesh 1 (M1, most refined), Mesh 2 (M2, moderately refined) and Mesh 3 (M3, coarse) for the RANS simulation, while the Navier–Stokes simulations use only Mesh 1. Tables A.1 and A.2 summarize the specific parameters associated with each mesh, along with the corresponding simulation results. The horizontal mesh resolution Δx is given in a range to reflect its gradual refinement closer to the object. The mesh in the region extending $2l$ ($\pm l$) (where l is the length of the object) from the object is non-uniform, with the smallest horizontal resolution indicated in the table as $\Delta_{\min}$. The non-dimensional wall-normal distance to the centre of the first grid cell $\overline{y^+}$, averaged in time and over the object's surface, is used to assess the near-wall mesh refinement. Convergence is evaluated based on the magnitude of surface elevations at points located $0.0155l$ from the object's front and back, as well as the forces in both directions. The magnitudes of these physical quantities are determined by averaging the signals over time after $t = 21T$ (where T represents the wave period), corresponding to the time at which a quasi-steady state is achieved. The first- and second-harmonic amplitudes of the quantities are computed using the Fast Fourier Transform (FFT) of the respective signals. Following the methodologies outlined by Stern et al. (2001) and Mohseni et al. (2018), the convergence study is carried out focusing on the first-harmonics.

As a measure of convergence, the convergence ratio $R = \dot{\epsilon}_{21}/\dot{\epsilon}_{32}$ is used, in which $\dot{\epsilon}_{ij} = \varphi_i - \varphi_j$ denotes changes to the solutions between Mesh i and Mesh j, with φ being the simulation result for any physical quantity of interest. For three sets of mesh, monotonic convergence is achieved when $R \in (0, 1)$, allowing for error estimation and uncertainty assessment through generalized Richardson Extrapolation (RE) (Liu et al., 2020). If we define the refinement ratio of the ith mesh to jth mesh as $\dot{r}_{ij} = \Delta_i/\Delta_j$, in which $\Delta = \Delta x = \Delta z$ is the mesh resolution on the free surface, then in both wave steepness cases, $\dot{r}_{21} = \dot{r}_{32} = 2$. The order of accuracy $\dot{m}$ for a constant refinement mesh ratio can be obtained by Roache (1994):

$$\dot{m} = \frac{\ln(\dot{\epsilon}_{32}/\dot{\epsilon}_{21})}{\ln(\dot{r})}. \tag{5}$$

Additionally, for a standard three-grid convergence study with an error estimated from RE, the Grid Convergence Index (GCI) approach is used with a safety factor F_S to indicate the uncertainty of the error estimate:

$$\mathrm{GCI}_{ij} = F_S \frac{|\epsilon_{ij}|}{\dot{r}_{ij} - 1}. \tag{6}$$

The results from this convergence analysis are detailed in Tables A.3 and A.4, where $F_S = 1.25$ for a minimum of three grids (Roache, 1994).

It is evident that for both the low- and high-wave steepness cases, overall, satisfactory convergence has been achieved for the quantities of interest, with minimal changes to the solution observed, particularly between Mesh 1 and Mesh 2. Analysis of the first-harmonic component reveals a small convergence ratio accompanied by a relatively high order of accuracy and a small GCI, indicating the simulated value is approaching the asymptotic range (Stern et al., 2001; Mohseni et al., 2018). Notably, for Mesh 1 and Mesh2, the time-averaged y^+ averaged over the body surface is below 1. Mesh 1 (the most refined mesh) is selected as the final mesh for all subsequent simulations.

Table A.1
Convergence study for low wave steepness ($ka_w = 0.034$), conducted at particle $\mathrm{Re}_x = 1.97 \times 10^4$, KC = 0.33. The mesh refinement is reduced in the order M1, M2, M3 with M3 being the most coarse mesh. N_c is the total number of cells in the mesh with the unit 'M' representing million. λ and l represent the wavelength and size of the object, respectively. Δx and Δz indicate the horizontal and vertical mesh sizes, while $\Delta_{\min}$ represents the smallest mesh size near the object surface. $\overline{y}^+$ is the time-averaged value of y^+ averaged over the object surface. a represents the local wave amplitude at the sampled location. The sample location 'Front' and 'Back' are chosen to lie a distance $0.0155l$ away from the front and back sides of the object. F_x and F_z are the magnitudes of the oscillatory parts of the horizontal and vertical forces, which are made non-dimensional as $F'_x = F_x/(\rho g a_w l^2/4)$ and $F'_z = F_z/(\rho g a_w l^2/4)$, respectively.

Simulation	Mesh	N_c	$\lambda/\Delta x$	$l/\Delta x$	$a_w/\Delta z$	$\Delta_{\min}$ (m)	$\overline{y}^+$	Front (a/a_w)	Back (a/a_w)	F'_x	F'_z
Navier–Stokes	M1	1.15M	185–7385	738	40	1.06×10^{-4}	0.37	1.74	0.59	2.02	1.00
RANS	M1	1.15M	185–7385	738	40	1.06×10^{-4}	0.35	1.75	0.57	2.03	1.03
	M2	0.69M	185–3693	369	20	2.11×10^{-4}	0.74	1.76	0.57	2.08	1.05
	M3	0.35M	185–1846	185	10	9.48×10^{-4}	2.77	1.92	0.55	2.24	1.11

Table A.2
Convergence study for the highest wave steepness ($ka_w = 0.09$) conducted at particle $\mathrm{Re}_x = 8.0 \times 10^4$, KC = 0.87. Mesh refinement is reduced in the order M1, M2, M3 with M3 being the most coarse mesh. N_c is the total number of cells in the mesh with the unit 'M' representing a million. λ and l are the wavelength and size of the object, respectively. Δx and Δz is the horizontal and vertical mesh sizes, while Δ_{min} represents the smallest mesh size near the object surface. $\overline{y}^+$ denotes the time-averaged value of y^+ averaged over the object surface. a represents the local wave amplitude at the sampled location. The sample location of 'Front' and 'Back' are chosen to lie a distance $0.0155l$ away from the front and back sides of the object. F_x and F_z are the magnitudes of oscillatory parts of the horizontal and vertical forces, which are made non-dimensional as $F'_x = F_x/(\rho g a_w l^2/4)$ and $F'_z = F_z/(\rho g a_w l^2/4)$, respectively.

Simulation	Mesh	N_c	$\lambda/\Delta x$	$l/\Delta x$	$a_w/\Delta z$	$\Delta_{\min}$ (m)	$\overline{y}^+$	Front (a/a_w)	Back (a/a_w)	F'_x	F'_z
Navier–Stokes	M1	1.04M	185–7385	738	106	1.05×10^{-4}	0.87	1.74	0.61	1.96	1.06
RANS	M1	1.04M	185–7385	738	106	1.05×10^{-4}	0.87	1.70	0.60	1.97	1.04
	M2	0.69M	185–3693	369	53	2.11×10^{-4}	1.81	1.71	0.60	1.97	1.04
	M3	0.35M	185–1846	185	27	4.47×10^{-4}	3.51	1.72	0.62	1.98	1.03

Table A.3
Convergence statistics of normalized first-harmonic components of target quantities for low wave steepness $ka_w = 0.034$ with particle $\mathrm{Re}_x = 3.01 \times 10^4$, KC = 0.34. F_{px} and F_{pz} are the magnitudes of the first-harmonics parts of the pressure forces on the object in the horizontal and vertical directions, respectively, and F_{vx} and F_{vz} are the magnitudes of the first-harmonics parts of the viscous forces on the object in the horizontal and vertical directions, respectively. All these forces shown with its non-dimensional form at the table are normalized by $F' = F/(\rho g a_w l^2/4)$.

Parameter	Front (a/a_w)	Back (a/a_w)	F'_{px}	F'_{pz}	F'_{vx}	F'_{vz}
M1	1.75	0.57	2.04	1.02	2.16×10^{-3}	2.02×10^{-3}
M2	1.76	0.57	2.09	1.03	2.16×10^{-3}	1.97×10^{-3}
M3	1.92	0.55	2.24	1.08	2.44×10^{-3}	1.47×10^{-3}
$\dot{\epsilon}_{21}$	0.01	-2.33×10^{-4}	0.05	0.01	5.01×10^{-6}	-4.82×10^{-5}
$\dot{\epsilon}_{32}$	0.16	−0.02	0.15	0.05	2.73×10^{-4}	-5.02×10^{-4}
R	0.06	0.01	0.33	0.29	0.02	0.10
$\dot{m}$	4.18	6.46	1.62	1.81	5.77	3.38
GCI_{21} [%]	1.09	0.03	6.24	1.65	6.26×10^{-4}	6.02×10^{-3}
GCI_{32} [%]	19.67	2.57	19.19	5.75	3.41×10^{-2}	6.27×10^{-2}

Table A.4
Convergence statistics of normalized first harmonic components of target quantities for highest wave steepness $ka_w = 0.09$ with particle $\mathrm{Re}_x = 8.0 \times 10^4$, KC = 0.9. F_{px} and F_{pz} are the magnitudes of the first-harmonics parts of the pressure forces on the object in the horizontal and vertical directions, respectively, and F_{vx} and F_{vz} are the magnitudes of the first-harmonics parts of the shear forces on the object in the horizontal and vertical directions, respectively. All these forces shown with its non-dimensional form at the table are normalized by $F' = F/(\rho g a_w l^2/4)$.

Parameter	Front (a/a_w)	Back (a/a_w)	F'_{px}	F'_{pz}	F'_{vx}	F'_{vz}
M1	1.73	0.53	1.99	0.96	2.26×10^{-3}	2.46×10^{-3}
M2	1.73	0.53	2.00	0.96	2.13×10^{-3}	2.32×10^{-3}
M3	1.75	0.55	2.00	0.96	1.79×10^{-3}	1.72×10^{-3}
$\dot{\epsilon}_{21}$	3.42×10^{-3}	3.84×10^{-3}	3.95×10^{-4}	-1.77×10^{-4}	-1.29×10^{-4}	-1.36×10^{-4}
$\dot{\epsilon}_{32}$	1.40×10^{-2}	1.78×10^{-2}	2.19×10^{-3}	-4.81×10^{-3}	-3.40×10^{-4}	-6.02×10^{-4}
R	0.24	0.22	0.18	0.04	0.38	0.23
$\dot{m}$	2.04	2.21	2.47	4.77	1.40	2.15
GCI_{21} [%]	4.27×10^{-3}	4.81×10^{-3}	0.05	0.02	0.02	0.02
GCI_{32} [%]	0.02	0.02	0.27	0.60	0.04	0.08

Appendix B. Validation and verification for small moving objects

Validation and verification of the QaleFOAM model are conducted by examining the drift of very small moving objects, focusing on Navier–Stokes and Euler simulations under low-wave steepness conditions. The suitability of the QaleFOAM model for wave-structure interaction problems has been demonstrated by comparison with experiments and other numerical models in Li et al. (2018), Yan et al. (2019) and Gong et al. (2020). Xiao et al. (2024a) showed that the QaleFOAM model correctly predicts the drift of infinitely small objects, i.e. fluid parcels, and very small objects with round corners and spherical shapes. Therefore, only simulations involving sharp-cornered boxes are presented here for brevity.

Experiments and theoretical models (Nath, 1978; van den Bremer et al., 2019; Calvert et al., 2021), show that when objects are very small, they behave as perfect Lagrangian tracer, rendering viscosity insignificant due to the very small relative velocity between the object and the surrounding fluid. Consequently, simulations for small objects are for very small particle Reynolds number ($|u_o - u_f| \to 0$), indicating a laminar flow regime around the object, although the flow itself could be turbulent. We have conducted RANS simulations but find very similar results to the Navier–Stokes simulations. For brevity, the RANS simulations are not presented here.

Table B.5
Results and mesh sensitivity study of a very small sharp-cornered box in low wave steepness $ka_w = 0.034$. For Euler simulations, the kinematic viscosity in the simulation is set as $\nu = 0$ and for Navier–Stokes simulations, $\nu = 1 \times 10^{-6}$ m^2 s^{-1}. The level of mesh refinement is reduced from M1 to M2, with M1 being the mesh used for later simulations. a is the wave amplitude at the downstream end of the tank, which is a good indicator of a clean wave field with minimal radiated and diffracted disturbances to the waves. u_O is the time-averaged horizontal drift velocity of the object. u_S is the standard Stokes drift calculated by (7) when $z = 0$. F_x and F_z are the magnitudes of the oscillatory parts of horizontal and vertical forces, which are made non-dimensional as $F'_x = F_x/(\rho g a_w l^2/4)$ and $F'_z = F_z/(\rho g a_w l^2/4)$.

Simulation	Mesh	l/λ	$\lambda/\Delta x$	$l/\Delta x$	$a_w/\Delta z$	N_c	a/a_w	u_O/u_S	F'_x	F'_z
Euler	M1	0.97	185–7385	72	40	0.38M	1.00	1.002	0.095	0.100
	M2	0.97	185–3692	36	20	0.24M	1.01	0.995	0.097	0.101
Navier–Stokes	M1	0.97	185–7385	72	40	0.38M	1.01	1.010	0.106	0.107
	M2	0.97	185–3692	36	20	0.24M	1.00	1.000	0.098	0.101

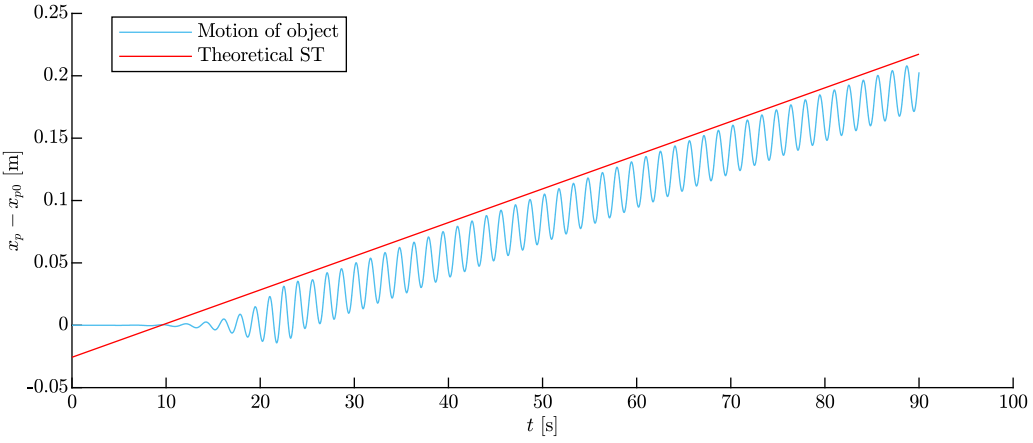

Fig. B.1. Time history of the horizontal motion of the small object in low-wave steepness waves ($ka_w = 0.034$) for Euler simulations. x_p is the time-dependent horizontal position of centre of mass of the object and x_{p0} is the initial horizontal position of its centre of mass.

In this section, we focus on a small sharp-cornered box with dimensions $l = 0.036$ m and $h_d = 0.025$ m. The results from Navier–Stokes and Euler simulations are given in Table B.5. The wave conditions are $\lambda = 3.69$ m, $a_w = 0.02$ m and $ka_w = 0.034$. Regarding the calculation of the (time-average) drift velocity, two methods are considered: processing the horizontal velocity using the Fast Fourier Transform (FFT) and applying a low-pass filter to obtain its subharmonic part (filtering out frequencies larger than 0.4 times the wave frequency) or applying a best linear fit over the horizontal trajectory to derive the mean velocity (Huang et al., 2011). Both methods yield similar results. We chose the latter approach as it allows potential future comparison with experimental data, where only the trajectory data is available. Following Xiao et al. (2024a), the time-averaged drift velocity of the object, denoted as u_O, is obtained by applying a best linear fit to the signal after reaching a quasi-steady state. Fig. B.1 provides an example of the drift trajectory obtained in the Euler simulation, demonstrating the achievement of a quasi-steady state around $t = 21T = 32$ s, leaving a duration of $39T$ for estimation of the time-averaged velocity. The wave amplitude a at a location far downstream near the outlet is calculated by averaging its wave amplitude over $39T$ after $t = 30$ s, as are the magnitudes of the oscillatory parts of forces F'_x and F'_z in both directions.

Fig. B.1 shows that except for the oscillatory motion, the object experiences a nearly constant mean drift that remains stable over $39T$ after $t = 32$ s. The observed drift follows the theoretical Stokes drift, thus confirming the accuracy of the Euler simulation. The leading-order theoretical expression for the Stokes drift u_S is:

$$u_S = {a_w}^2 \omega_e k e^{2kz}, \tag{7}$$

The data in Table B.5 corroborates this finding, indicating that for the Euler simulation, the mean drift velocity closely aligns with the theoretical Stokes drift. Moreover, in the Navier–Stokes simulations incorporating viscosity, the small object follows Lagrangian drift behaviour, validating the efficacy of the Navier–Stokes simulations. In addition, Table B.5 shows that the quantities of interest exhibit minimal sensitivity to the mesh resolution. It is important to note that verification and validation of the model, including the convergence test and the validation of the small objects, only cover partly the validation process. Ideally, the comparisons of the trajectories of large objects to the experiment should be conducted in the future to further validate the simulations presented here. Also, the comparison of the vorticity structures and patterns that we observe (reported in Section 3.1.2) with the relevant data/results should be conducted for comprehensive validation.

Appendix C. Additional analysis for stationary objects

In this appendix, we provide additional analysis for the stationary objects to complement the discussions in Section 3.2.

C.1. The values of y^+, particle Reynolds number and keulegan–carpenter number

Fig. C.2 gives the y^+ distribution over the object boundaries for the lowest and highest wave steepness values in the RANS simulations. It demonstrates that the current mesh used ensures that most of the mean value of y^+ across all boundaries remains smaller than 1 except for very small parts on AB for the highest wave steepness are larger than 1 where the region is either on the air phase or near the free surface. Suffice to say, the mesh used is sufficient for the wall-resolving models. The corresponding particle Reynolds numbers and Keulegan–Carpenter (KC) numbers are given in Table C.6. Compared to the moving object, both particle Reynolds numbers and Keulegan–Carpenter numbers for stationary objects fall within the same flow regimes but have slightly larger values, leading to larger regions where vortex and wake structures are observed.

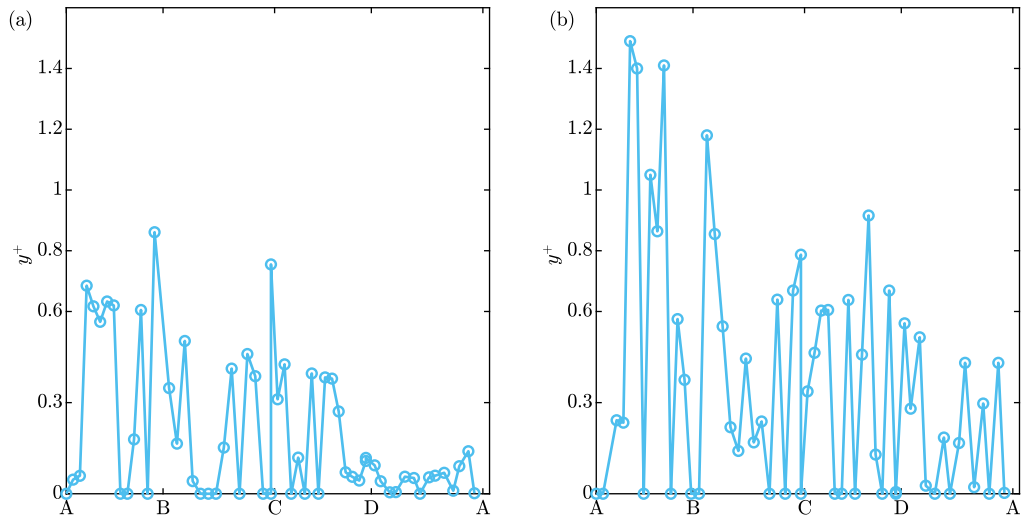

Fig. C.2. Time-averaged y^+ distribution over the edges of the stationary object for two values of wave steepnesses for the RANS simulations of a sharp-cornered box. (a) $ka_w = 0.034$, (b) $ka_w = 0.09$.

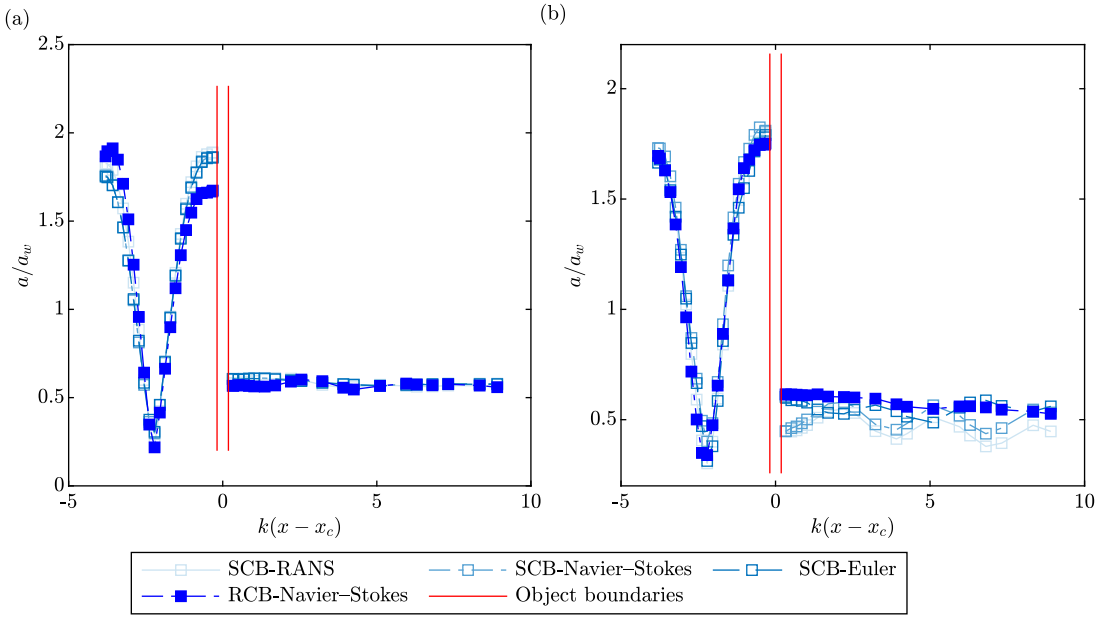

Fig. C.3. Standing wave pattern: amplitude of local wave surface elevation $a(x)$ as a function of horizontal distance from the centre of mass x_c for a stationary object of relative size $l/\lambda = 10\%$ with two different corner shapes. (a) different types of simulation in low wave steepness $ka_w = 0.034$, (b) different types of simulation in high wave steepness $ka_w = 0.09$. The local wave amplitude $a(x)$ is normalized by incoming wave amplitude a_w and the horizontal distance is scaled by the wavenumber. The object boundaries represent the left and right sides of the object.

Table C.6
Particle Reynolds and Keulegan–Carpenter numbers for stationary objects for different wave steepness. The values of Reynolds and Keulegan–Carpenter numbers are the identical for sharp-cornered and round-cornered boxes.

ka_w	l/λ (%)	Re_x ($\times 10^4$)	KC
0.03	10.0	1.97	0.33
0.07	10.0	6.18	0.67
0.09	10.0	7.99	0.87

C.2. Standing wave pattern

We conducted a wave-field analysis to examine wave diffraction effects on the stationary objects. The results are shown in Fig. C.3 for $ka_w = 0.034$ and $ka_w = 0.09$. For low wave steepness, in line with the observations in Section 3.1.1, the sharp-cornered boxes induce a larger standing wave pattern compared to the round-cornered boxes, with no significant variation across different simulation types. For high wave steepness, however, the difference between the two types of objects diminishes noticeably. Furthermore, it is observed that the normalized wave pattern in high wave steepness (maximum $a/a_w = 1.8$) is smaller than that for low wave steepness (maximum $a/a_w = 2.0$). This finding aligns with the conclusions drawn by Xiao et al. (2024a), indicating that as the wave steepness increases, the standing wave pattern normalized by wave amplitude decreases, resulting in smaller drift amplification factor.

C.3. Spectral analysis of turbulent kinetic energy

To analyse the turbulent statistics in the fluid field around the object, we conduct a spectral analysis of the turbulent kinetic energy k_e based on the time history collected at the sampling points in the fluid

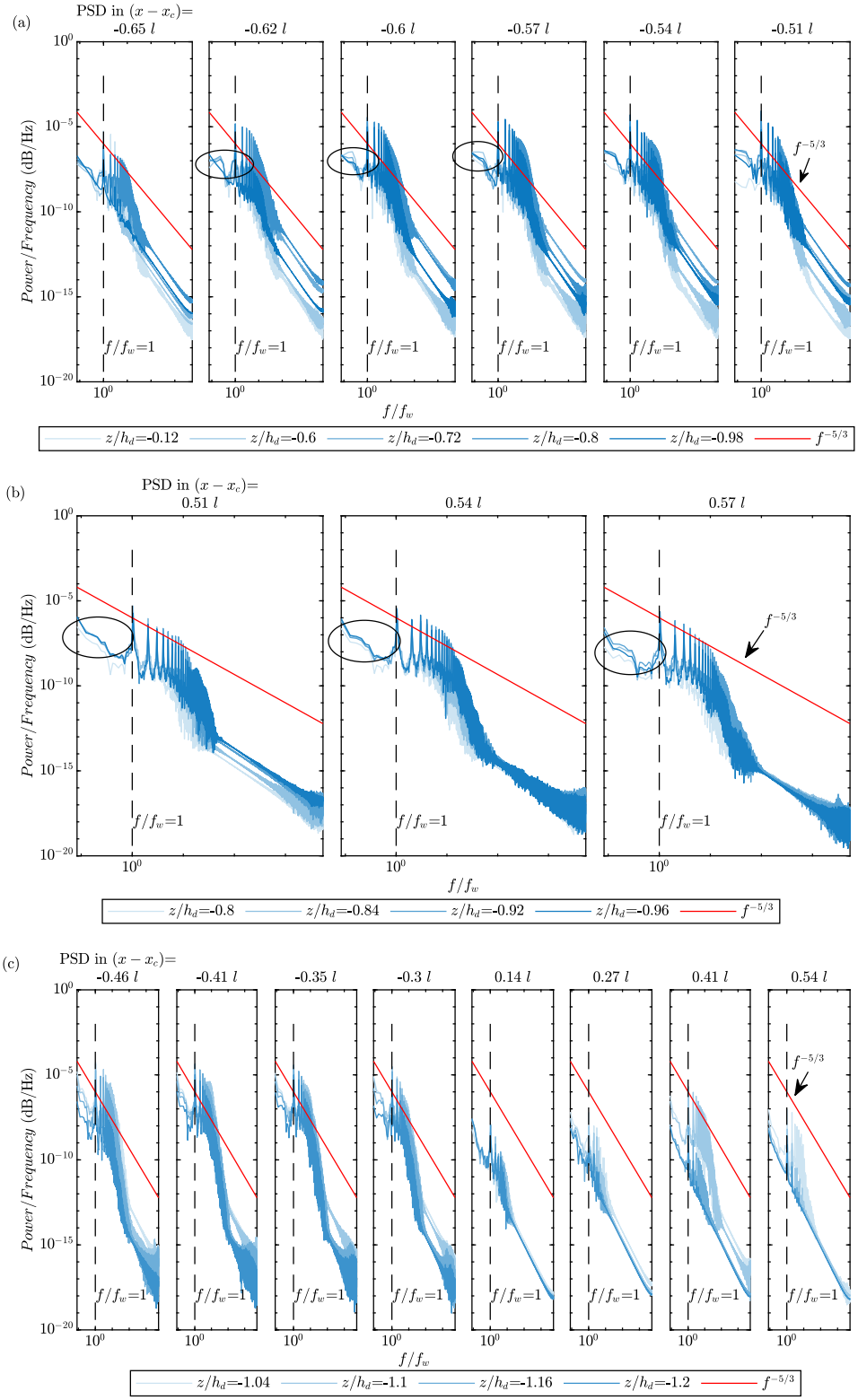

Fig. C.4. Power spectral density (PSD) of turbulent kinetic energy (TKE) k_e at sampling points in the fluid field around the object for RANS simulations of stationary objects ($l/\lambda = 10\%$) with sharp corners when $ka = 0.034$. (a) left (front region) (b) rear (right) region (c) bottom region. The red lines represent the theoretical lines of Kolmogorov's 5/3 law in the inertial subrange. The left and right boundaries of the object are located at $x - x_c = -0.5l$ and $x - x_c = 0.5l$, respectively. The bottom boundaries are located at $z/h_d = 1$, $x - x_c = [-0.5l, 0.5l]$.

field defined in Table 6. The power spectral density of k at left (front), bottom and right (rear) regions is presented in Fig. C.4. We selectively chose sampling points within regions where vorticity is pronounced, resulting in uneven distributions at the upstream and downstream regions. For the left region, where vorticity is generated and covers $0.13l$, turbulent energy k_e is observed to follow Kolmogorov's 5/3

law. As points move closer to the object, the power spectral density of k_e increases, indicating a more turbulent fluid field. Notably, at $x = -0.65l$, turbulent energy is only observed at locations $z = -0.72h_d$ and $z = -0.8h_d$, while points closer to the object exhibit more turbulent energy distribution. For points located at $x - x_c = -0.52l$, that is just $0.015l$ from edge AD (the left edge of the object), the turbulent region spans the entire sampling region $-0.12h_d \leq z \leq 1$. Compared to the upstream side, the downstream side contains less turbulent energy, with the turbulent region spanning a smaller horizontal and vertical extent.

To be more specific, the region in the downstream side spans from $0.05l$ horizontally and $0.2h_d$ vertically (vs. $0.13l$ horizontally and $0.88h_d$ vertically for the upstream side). In the bottom region, points on the left side accumulate more turbulent energy and have a larger vertical span compared to the right side region. In addition to the turbulent energy peak at the frequencies $f/f_w \geq 1.0$ Hz, there is a large amount of turbulent energy for $f/f_w \leq 1.0$ Hz. There is an area for $f/f_w \leq 1.0$ Hz that gains local increase as frequency increases (outlined by ellipse in the corresponding figures) in the left region of which the pattern is not observed in the right region. Because those frequencies are lower than the frequency of objects' linear motion (equal to the incident wave frequency), it induces more sub-harmonic disturbance for the object's drift, which might help to explain the unsteadiness and time-decaying components found in Section 3.1.2.

References

Bearman, P.W., Graham, J.M.R., Obasaju, E.D., Drossopoulos, G.M., 1984. The influence of corner radius on the forces experienced by cylindrical bluff bodies in oscillatory flow. Appl. Ocean Res. 6 (2), 83–89.

Bøckmann, A., Pâkozdi, C., Kristiansen, T., Jang, H., Kim, J., 2014. An experimental and computational development of a benchmark solution for the validation of numerical wave tanks. In: International Conference on Offshore Mechanics and Arctic Engineering. vol. 45400, American Society of Mechanical Engineers, V002T08A092.

Calvert, R., McAllister, M.L., Whittaker, C., Raby, A., Borthwick, A.G.L., van den Bremer, T.S., 2021. A mechanism for the increased wave-induced drift of floating marine litter. J. Fluid Mech. 915.

Chen, X., Xia, H., 2017. A hybrid LES-RANS study on square cylinder unsteady heat transfer. Int. J. Heat Mass Transfer 108, 1237–1254.

Danmeier, D.G., Seah, R.K.M., Finnigan, T., Roddier, D., Aubault, A., Vache, M., Imamura, J.T., 2008. Validation of wave run-up calculation methods for a gravity based structure. In: International Conference on Offshore Mechanics and Arctic Engineering. vol. 48234, pp. 265–274.

Deike, L., Pizzo, N., Melville, W.K., 2017. Lagrangian transport by breaking surface waves. J. Fluid Mech. 829, 364–391.

Delany, N.K., Sorensen, N.E., 1953. Low-Speed Drag of Cylinders of Various Shapes. Technical Report 3038, National Advisory Committee for Aeronautics..

DiBenedetto, M.H., Clark, L.K., Pujara, N., 2022. Enhanced settling and dispersion of inertial particles in surface waves. J. Fluid Mech. 936, A38.

Eeltink, D., Calvert, R., Swagemakers, J.E., Xiao, Q., van den Bremer, T.S., 2023. Stochastic particle transport by deep-water irregular breaking waves. J. Fluid. Mech. 971, A38.

Gong, J., Yan, S., Ma, Q.W., Li, Y., 2020. Added resistance and seakeeping performance of trimarans in oblique waves. Ocean Eng. 216, 107721.

Grue, J., Kolaas, J., 2017. Experimental particle paths and drift velocity in steep waves at finite water depth. J. Fluid Mech. 810.

Hu, J.C., Zhou, Y., Dalton, C., 2006. Effects of the corner radius on the near wake of a square prism. Exp. Fluids 40 (1), 106–118.

Huang, J., Carrica, P.M., Stern, F., 2008. Semi-coupled air/water immersed boundary approach for curvilinear dynamic overset grids with application to ship hydrodynamics. Int. J. Numer. Methods Flow 58 (6), 591–624.

Huang, G., Law, A.W., Huang, Z., 2011. Wave-induced drift of small floating objects in regular waves. Ocean Eng. 38 (4), 712–718.

Inoue, M., Baba, N., Himeno, Y., 1993. Experimental and numerical study of viscous flow field around an advancing vertical circular cylinder piercing a free-surface. J. the Kansai Soc. Nav. Archit. Jpn. 220, 57–64, in Japanese.

Kandasamy, M., Xing, T., Stern, F., 2005. Unsteady free-surface wave induced separation: coherent vortical structures and instabilities. J. Fluid. Struct..

Kawamura, T., Mayer, S., Garapon, A., Sørensen, L., 2002. Large eddy simulation of a flow past a free surface piercing circular cylinder. J. Fluids Eng. 124 (1), 91–101.

Li, Q., Wang, J.H., Yan, S.Q., Gong, J.Y., Ma, Q.W., 2018. A zonal hybrid approach coupling FNPT with OpenFOAM for modelling wave-structure interactions with action of current. Ocean. Syst. Eng. 8 (4), 381–407.

Liang, Y., Tao, L., Xiao, L., Liu, M., 2016. Experimental and numerical study on flow past four rectangular columns in diamond configuration. In: International Conference on Offshore Mechanics and Arctic Engineering. vol. 49927, American Society of Mechanical Engineers, V001T01A044.

Lin, P., Li, C.W., 2003. Wave–current interaction with a vertical square cylinder. Ocean Eng. 30 (7), 855–876.

Liu, Z.H., Zhuang, Y., Wan, D.C., 2020. Numerical study of focused wave interactions with a single-point Moored hemispherical-bottomed buoy. Int. J. Offshore Polar 30 (01), 53–61.

Longuet-Higgins, M.S., 1953. Mass transport in water waves. Philos. Trans. R. Soc. A 245 (903), 535–581.

Lyn, D.A., Einav, S., Rodi, W., Park, J.H., 1995. A laser-Doppler velocimetry study of ensemble-averaged characteristics of the turbulent near wake of a square cylinder. J. Fluid Mech. 304, 285–319.

Mohseni, M., Esperanca, P.T., Sphaier, S.H., 2018. Numerical study of wave run-up on a fixed and vertical surface-piercing cylinder subjected to regular, non-breaking waves using openFOAM. Appl. Ocean Res. 79, 228–252.

Moradi, N., Zhou, T., Cheng, L., 2015. Effect of inlet configuration on wave resonance in the narrow gap of two fixed bodies in close proximity. Ocean Eng. 103, 88–102.

Nath, J.H., 1978. Drift speed of buoys in waves, with appendix by MS Longuet–Higgins. Coast. Eng. Proc. 1 (16), 49–49.

Palm, J., Eskilsson, C., Bergdahl, L., Bensow, R.E., 2018. Assessment of scale effects, viscous forces and induced drag on a point-absorbing wave energy converter by CFD simulations. J. Mar. Sci. Eng. 6 (4), 124.

Palm, J., Eskilsson, C., Paredes, G.M., Bergdahl, L., 2016. Coupled mooring analysis for floating wave energy converters using CFD: Formulation and validation. Int. J. Mar. Energy 16, 83–99.

Roache, P.J., 1994. Perspective: A method for uniform reporting of grid refinement studies. J. Fluid. Eng. (United States) 116 (3).

Roshko, A., 1952. On the Development of Turbulent Wakes from Vortex Streets (Ph.D. thesis). California Institute of Technology.

Sinnis, J.T., Grare, L., Lenain, L., Pizzo, N., 2021. Laboratory studies of the role of bandwidth in surface transport and energy dissipation of deep-water breaking waves. J. Fluid Mech. 927, A5. http://dx.doi.org/10.1017/jfm.2021.734.

Spalart, P.R., 1998. Airplane trailing vortices. Annu. Rev. Fluid Mech. 30, 107.

Stansberg, C.T., Baarholm, R., Kristiansen, T., Hansen, E.W.M., Rortveit, G., 2005. Extreme wave amplification and impact loads on offshore structures. In: Offshore Technology Conference. OTC, pp. OTC–17487.

Stansberg, C.T., Kristiansen, T., 2005. Non-linear scattering of steep surface waves around vertical columns. Appl. Ocean Res. 27 (2), 65–80.

Stansberg, C.T., Nielsen, F.G., 2001. Nonlinear wave-structure interactions on floating production systems. In: ISOPE International Ocean and Polar Engineering Conference. ISOPE, ISOPE–I.

Stern, F., Wilson, R.V., Coleman, H.W., Paterson, E.G., 2001. Comprehensive approach to verification and validation of CFD simulations—part 1: methodology and procedures. J. Fluids Eng. 123 (4), 793–802.

Stokes, G.G., 1847. On the theory of oscillatory waves. Trans. Camb. Phil. Soc. 8, 411–455.

Sumer, B.M., et al., 2006. Hydrodynamics Around Cylindrical Structures, vol. 26, World scientific.

Tamura, T., Miyagi, T., 1999. The effect of turbulence on aerodynamic forces on a square cylinder with various corner shapes. J. Wind Eng. Ind. Aerodyn. 83 (1–3), 135–145.

Tamura, T., Miyagi, T., Kitagishi, T., 1998. Numerical prediction of unsteady pressures on a square cylinder with various corner shapes. J. Wind Eng. Ind. Aerodyn. 74, 531–542.

Tong, F., Cheng, L., Xiong, C., Draper, S., An, H., Lou, X., 2017. Flow regimes for a square cross-section cylinder in oscillatory flow. J. Fluid Mech. 813, 85–109.

Van den Bremer, T.S., Breivik, Ø., 2018. Stokes drift. Phil. Trans. R. Soc. A 376 (2111), 20170104.

van den Bremer, T.S., Whittaker, C., Calvert, R., Raby, A., Taylor, P.H., 2019. Experimental study of particle trajectories below deep-water surface gravity wave groups. J. Fluid. Mech. 879, 168–186.

Wiliamson, C.H., 1996. Vortex dynamics in the cylinder wake. Annu. Rev. Fluid Mech. 28 (1), 477–539.

Xiao, Q., Calvert, R., Yan, S.Q., Adcock, T.A.A., van den Bremer, T.S., 2024a. Surface gravity wave-induced drift of floating objects in the diffraction regime. J. Fluid Mech. 980, A27.

Xiao, Q., McAllister, M., Adcock, T., van den Bremer, T., 2024b. Laboratory study of wave-induced drift of large floating objects. In: International Workshop on Water Waves and Floating Bodies. International Workshop on Water Waves and Floating Bodies.

Yan, S., Ma, Q.W., Wang, J., Wang, J., 2019. Numerical modelling of wave resonance in a narrow gap between two floating bodies in close proximity using a hybrid model. In: International Conference on Offshore Mechanics and Arctic Engineering. vol. 58882, American Society of Mechanical Engineers, V009T12A009.

Yang, S., Luo, S., Liu, F., Tsai, H., 2007. Euler solutions of flow around a rectangular wing with square tip. In: 45th AIAA Aerospace Sciences Meeting and Exhibit. p. 896.

Yen, S.C., Yang, C.W., 2011. Flow patterns and vortex shedding behavior behind a square cylinder. J. Wind Eng. Ind. Aerodyn. 99 (8), 868–878.

Yoon, S.H., Kim, D.H., Sadat-Hosseini, H., Yang, J., Stern, F., 2016. High-fidelity CFD simulation of wave run-up for single/multiple surface-piercing cylinders in regular head waves. Appl. Ocean Res. 59, 687–708.
Yoon, D.H., Yang, K.S., Choi, C.B., 2010. Flow past a square cylinder with an angle of incidence. Phys. Fluids 22 (4), 043603.
Yu, Y.H., Li, Y., 2013. Reynolds-averaged Navier–Stokes simulation of the heave performance of a two-body floating-point absorber wave energy system. Comput. & Fluids 73, 104–114.